CATHODOLUMINESCENCE SPECTROSCOPY OF ORGANIC-INORGANIC PEROVSKITES

LEW KAR CHENG

DIVISION OF PHYSICS & APPLIED PHYSICS
SCHOOL OF PHYSICAL AND MATHEMATICAL SCIENCES

A thesis submitted to the Nanyang Technological University
in partial fulfilment of the requirement for the degree of
Master of Science

2017

Acknowledgements

I would like to express my sincere gratitude to my supervisor, Assoc. Prof. Cesare Soci, for introducing me to this field of photophysics and providing me great environment with advanced facilities.

I am grateful to have Mr. Daniele Cortecchia involved in this project because he is an expert in perovskites. He has paid high contribution in this project, typically on the synthesis of the perovskite materials. Without his passionate participation and advices, this project would not be conducted successfully.

I also greatly appreciate the guidance from Dr. Jin-kyu So throughout this year. He has provided me trainings on the usage of cathodoluminescence system, and making sure that the cathodoluminescence system is well maintained. I sincerely thank him for his help, patience and comprehension along this project. Besides that, another notable mention to Dr. Annalisa who has trained me on photoluminescence equipment.

Thanks to all the group members of OSON and CDPT for making this joyful year. Thanks to my friends, Shu Tian, Han Kheng, Wui Seng and Jun Onn who have had countless meals and jokes with me. Thanks to my beloved partner, Aaron, who has been encouraging me continuously and sharing values of life with me.

Finally, I must thank my family who has always respected my every decision and been very supportive.

Table of Contents

Abstract

In this work, cathodoluminescence (CL) techniques was applied to hybrid perovskite materials to identify relationship between their crystallographic microstructure and emission properties. The cathodoluminescence spectra of $MAPbI_3$ and $CsPbBr_3$ were compared against conventional photoluminescence spectra. Furthermore, interesting quasi two-dimensional organic-inorganic perovskites were studied with this technique. A bulky cation phenylethylammonium (PEA=$C_8H_9NH_3$) was used to induce the formation of layered perovskites of the Ruddlesden-Popper series, and the dimensionality (n) of the resulting $(PEA)_2(MA)_{n-1}$ $[Pb_nI_{3n+1}]$ was tuned by adjusting the ratio of methylammonium iodide to PEA iodide. Steady-state and fast (ps) time-resolved cathodoluminescence spectroscopy were employed for the first time to correlate spatially resolved yield and dynamics of the luminescence with the complex phase distribution of multidimensional perovskite polycrystalline film. It was found that phase separation occurs into two preferential domains, corresponding to low- and high-dimensional perovskite rich areas. In this film, charge transfer and energy funnelling effects allow compositional control of the emission energy and recombination dynamics.

Introduction

Cathodoluminescence studies of perovskite

Organic-inorganic hybrid perovskites are semiconducting compounds which combine the electronic and charge transport properties of conventional inorganic semiconductors with the processing advantages of organic semiconductors, which can be prepared in at high yield and low cost. Since they can be fabricated at low cost and in relatively easy ways, they have attracted vast interest for applications.

Within the past few years, the thin film of perovskites has exhibited exceptional solar cell efficiencies 22.1 %, which are now comparable to silicon solar cells in crystalline form 27.6% (Figure 1) [1]. Besides that, with the properties of efficient light emitters, perovskites have also enhanced the development of optoelectronic application such as light-emitting devices(LED) [2] and optically pumped tunable laser [3]. The transport properties such as mobility and the lifetime of the charge carriers within these materials are measured to be high [4,5], however, they are still not well understood. One of the keys to understanding the charge transport properties is the study of “excitons”, a quasiparticle which is the bound state of the electron and hole. The electron and hole recombine to give rise to electro-luminescence. Organic cation drift is believed to act as an important role on the charge transport properties in organic-lead halide perovskite. Emission properties of these materials are related to the film morphology, composition, crystallographic phase and defects, which typically occur at sub-micron scale. Hence, spectroscopic technique such as cathodoluminescence with high resolution may be a valuable tool to elucidate structure-luminescence properties relationships in this class of materials.

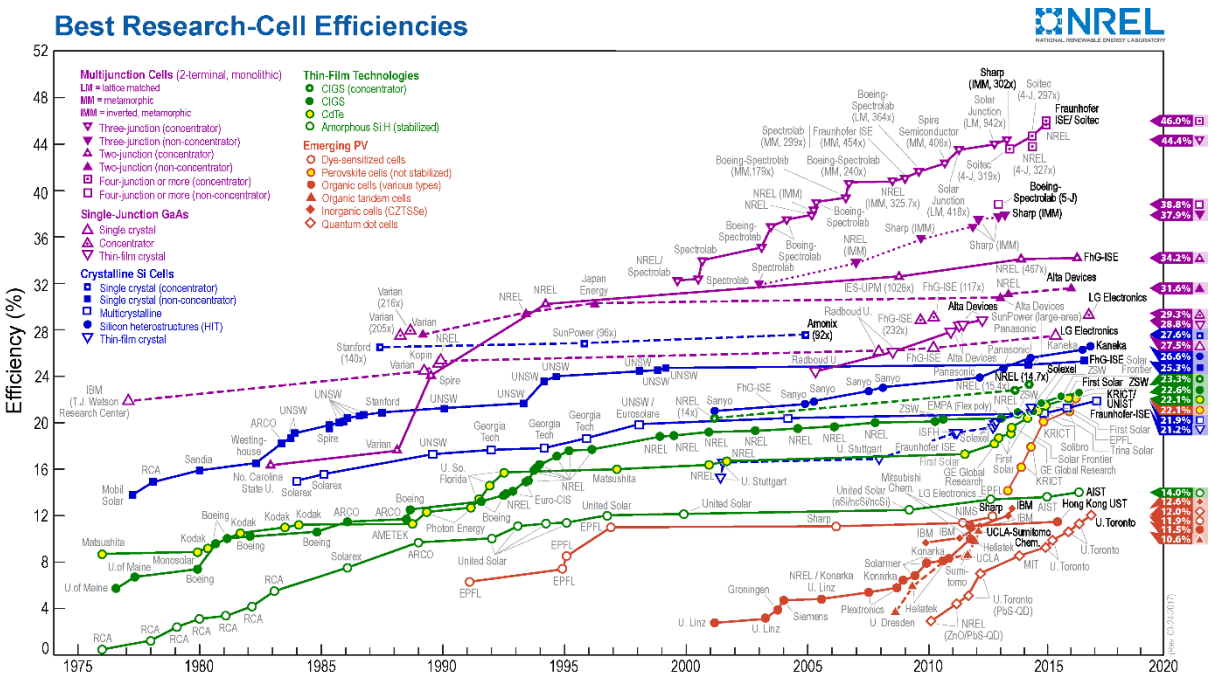

Figure 1. Development of research-cell efficiencies through decades [1].

Cathodoluminescence (CL) is the emission of photons that results from electrons striking a material. This is a phenomenon that combines electromagnetic and optical effects. It seems as the reverse process of the photoelectric effect (in which photons induce the the emission of electrons), the emission of photons is induced by an electron beam in CL.

CL was discovered relatively late compared to other luminescences such as photoluminescence and chemiluminescence because it requires a vacuum environment and a high concentration of electrons. The discovery of cathode ray in the 19th century aroused the curiosity of J.J. Thompson, leading to his discovery of electrons in 1897 [6]. One of the most significant attributes of CL is a cathode ray tube (CRT) which is able to produce images by controlling the intensities and the directions of the electron beams [7]. This technology was applied in a number of instruments such as electronic televisions, computer displays and oscilloscopes. With the development of electron microscopy technologies, scientists were able to analyse luminescent materials with CL

phenomenon. This was completed with the installation of a luminescence detector into the scanning electron microscope (SEM) which also operates with electrons bombardment. This becomes an important characterization tool for scientists to understand luminescent materials at microscopic levels. Cathodoluminescence of a material or semiconductor can provide unique insight into the chemical and optoelectronic properties of the material at microscopic level. For instance, by measuring the concentration and distribution of luminescence, the composition of compound materials can be determined [8]. The electronic properties that are determined by CL, such as carrier diffusion length and rate of surface recombination by varying electron beam voltage, play main roles in understanding the mechanism of generation and transport of charge carriers.

Furthermore, cathodoluminescence technique has been used to study plasmon excitations in metals [9]. Over the last decades, several works have shown that plasmons could be resolved spatially in nanostructures, including localized plasmon modes in gold nanoparticles [10], plasmon standing waves in gold gratings [11], hyperspectral imaging of nanowires [12] and particle dimers [13]. Overall, cathodoluminescence is a unique technique in analysis of surface plasmon polariton (SPP) and local plasmon resonance (LPR), providing an actual visualization of the electric field distribution in nanostructures with nanometre resolution.

The latest breakthrough in CL spectroscopy has been achieved in the last decade with the advent at time-resolved cathodoluminescence (TRCL) methods, which hold ultrafast (ps) time domain to enhance the overall capabilities of this technique. In most cases, the spatial resolution of conventional time-resolved photoluminescence (TRPL) systems is limited to only few microns. Hence, the optical PL spectroscopy of inhomogeneous substances only provides information that is integrated over a large spectral domain, and

cannot differentiate between local processes such as radiative processes and, carrier transfer among different radiative or nonradiative centre. Moreover, such information is not detailed enough to characterize an individual nano-sized object. To overcome these limitations, strongly localized excitation is achievable in a time-resolved cathodoluminescence (TRCL) system. TRCL can isolate luminescence phenomena both spatially and spectrally, and yield their dynamic characteristics separately. For instance, the lifetime of the minority carriers or nano-sized object can be determined by TRCL spectroscopy. By far, there is very limited amount of research that has applied cathodoluminescence technique to perovskite materials, especially TRCL. For instance, only steady-state CL spectroscopy was done on $MAPbI_3$, $FAPbI_3$ and $CsPbI_3$ [14,15] and CL mapping was done on $MAPbI_3$[16,17]. Therefore, it was decided to employ such unique technique capability to reveal the spatial distribution of emission from perovskites of different kinds with a combination of steady-state and time-resolved modes.

Purposes of this research

This research project aims to study the exciton and charge dynamics in hybrid organic-inorganic perovskite using cathodoluminescence spectroscopy, ultrafast spectroscopy and microscopy, hence identify ways of enhancing the mobility of the charge carriers in perovskite materials and improving their radiative emission properties for light emission applications. Overall, this work will contribute to both, the understanding of fundamental properties of this fascinating class of materials, and the development of perovskite devices for emerging applications.

Organization of this report

This report starts with several descriptions about the origin of CL signals from semiconductors in Chapter 1. Some important concepts such as interaction between electrons and atoms of the material, excitation energy states transition and vibrational states transitions are mentioned. Some concepts related to energy transition in molecules are also introduced.

Chapter 2 describes the materials inspected in preliminary research experiments. It introduces the structures and properties of perovskite materials. Different classes of hybrid perovskite materials were chosen to be studied due to their unique luminescence properties. The syntheses of these perovskites were also described.

Next, Chapter 3 includes the experimental methods, such as optical characterization methods and cathodoluminescence characterization methods. The working principles of the steady-state and time-resolved CL system, including details of the instrumental setup were described. Next, the reviews of the methodology adapted in this study are described. The synthesis of perovskites and the methods of characterization such as absorption and photoluminescence spectra acquisition are described in this chapter.

In Chapter 4, results on optical and cathodoluminescence characterization of perovskites are given. CL spectra and mapping of standard perovskites and hybrid perovskites of Ruddlesden-Popper series were measured, showing the capability of high spatial resolution of the CL technique. Besides that, time-resolved CL and time-resolved PL measurements on these perovskites were performed and compared, elucidating the energy funnelling effect occurs in quasi two-dimensional Ruddlesden-Popper series perovskite thin films.

Chapter 5 concludes and summarize this project whereas the final chapter provides several suggestions for future work. Nanostructured perovskites and nanopatterned (metamaterial) perovskites can be the options for future research, followed by advanced measurement modes, including Electron-beam-induced current (EBIC) and probably time-resolved EBIC measurements.

Chapter 1

Cathodoluminescence in Semiconductor and Cathodoluminescence Technique

1.1 Interaction between electrons and materials

Electron microscopy becomes one of the most popular instrumental techniques in investigating the morphology of materials in high resolution. Electron microscopy has much higher resolution than optical microscopy because the De-Broglie wavelength of electrons can be up to 100,000 times shorter than that of visible photons ($\lambda_{shortest} = 400nm$). This can significantly reduce the Abbe diffraction limit:

$$Resolvable\ feature\ size, d = \frac{\lambda}{2\ NA} \tag{1.1}$$

where λ is wavelength and NA is the numerical aperture of the objective lens.

When an electron beam strikes on a solid, it penetrates through its surface then interacts with bulk atoms. Different interactions can occur simultaneously, as summarized in Figure 1-1. The most elementary process is the collision of electron and electron or nucleus of an atom. These interactions can be classified into elastic interactions and inelastic interactions:

(i) Elastic interactions

There is no energy transfer between the incident electron and the atom. The first case is there is no interaction between the incident electrons and atoms, so the electron beam passes through the sample in the direction of incident

beam. Another case happens when the electron is deflected without significant energy loss whereas nucleus remains its position because nucleus is much heavier than electron. These elastically scattered electrons are commonly ejected back, namely backscattered electrons (BE) whose energy is comparable to that of incident electrons.

(ii) Inelastic interactions

These interactions mostly occur between the incoming electrons and the bounded electrons because they have equal masses. The energy of the incoming electron is transferred to the specimen, inducing different signals such as X-rays, secondary electrons, Auger electrons and importantly for us, cathodoluminescence (photons).

It is crucial to mention that most of the energy of the electron beam is absorbed by the material and converted into heat energy, generating phonons [18].

Depending on the energy of the impinging electrons and the resulting penetration depth, different processes may occur, as depicted in Figure 1-1. The cathodoluminescence signal of interest is emitted from deeper section levels in term of excitation volume. Due to large interaction volume, CL is useful to investigate defects. The nature of cathodoluminescence of a material is a complex function of lattice structure, composition, morphology and strain or damage on the structure of the material.

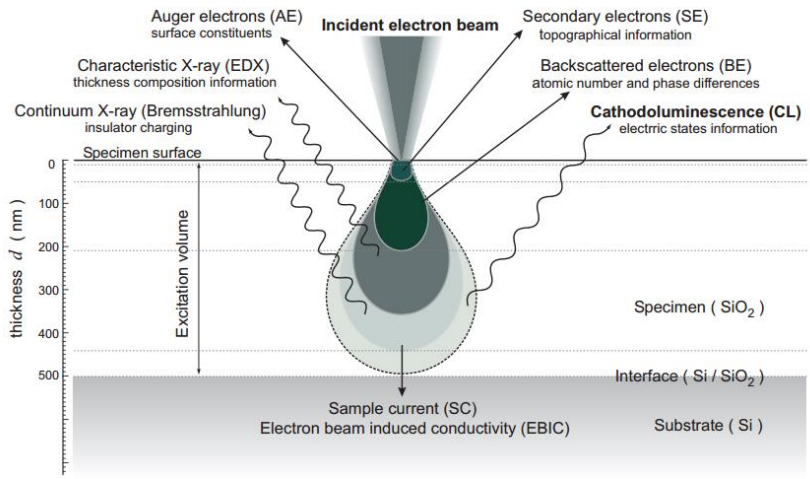

Figure 1-1. Scheme of electron-matter interactions under the impact of electron beam [19].

There are several ways of modelling the elastic and inelastic scattering that occurs in a specimen due to electron beam penetration, such as Monte Carlo simulation [20] and analytical study. The depth of electron penetration x_e (in μm) was approximated to be:

$$x_e \cong \frac{0.1\ E_0^{1.5}}{\rho} \tag{1.2}$$

where E_0 is incident energy (in keV) and ρ is density of the sample (in kg/m^3) [21]. The excitation volume which results from the scattering by collisions was approximated to be:

$$y_e \cong \frac{0.077\ E_0^{1.5}}{\rho} \tag{1.3}$$

where y_e is the width of the excitation volume (in μm) [21]. This should be taken into account when interpreting cathodoluminescence emission zone as a function of electron beam energy.

1.2 Energy of excitation electron beam

De-Broglie relation states that a moving charged particle has dual identity: wave and particle. Hence, a moving electron can also be treated as a radiation with wavelength λ:

$$De - Broglie\ wavelength, \lambda = \frac{h}{p} = \frac{h}{mv} \tag{1.4}$$

where h is the Planck constant, p is the momentum of the electron with mass m moving with velocity v. The velocity β, in unit of speed of light c, of an electron which is accelerated by voltage V can be expressed in equation (1.5).

$$\beta = \frac{v}{c} = \sqrt{1 - \frac{1}{\left(1 + \frac{eV}{m_e c^2}\right)^2}} \tag{1.5}$$

where m_e represents the rest mass of electron and e represents the charge of electron.

The mass of a moving electron, m, is shown in equation (1.6). The relationship between accelerating voltage and electron wavelength is simplified to equation (1.7). Table 1 contains the values of electron velocity and wavelength for different accelerating voltage.

$$m = \frac{m_e}{\sqrt{1 - \beta^2}} \tag{1.6}$$

$$\lambda = \frac{1.23}{\sqrt{V}} \tag{1.7}$$

It is apparent that the diffraction limit (wavelength) is smaller when higher accelerating voltage applied, however, high accelerating voltage will introduce high energy and may destroy the material. Therefore, in spatially resolved CL measurements, the lowest accelerating voltages are typically chosen, compatibly with the signal-to-noise ratio.

This is to optimize the spatial resolution which is given by:

$$d = \frac{0.613}{\alpha \cdot \sqrt{V}} \tag{1.8}$$

where d is the resolution of electron microscope (in nm), α is the half opening angle of the objective (in $radian$) and V is the accelerating voltage (in eV).

Table 1-1. The wavelength and velocity of electron under various accelerating voltages.

Accelerating voltage (kV)	**Electron velocity in units of speed of light, β**	**Electron wavelength, λ (nm)**
1	0.062	0.0388
5	0.139	0.0173
10	0.195	0.0122
20	0.272	0.0086
50	0.412	0.0054

1.3 Electron-beam-induced light emission

The mechanisms of photon emission induced by electron bombardment can be classified according to their degree of coherence with respect to the external evanescent field accompanying the moving charge. Note that coherent electron radiation is dominant mechanisms in metals whereas the incoherent cathodoluminescence is dominant emission in semiconductors. In this research, incoherent cathodoluminescence (recombination emission) of perovskite materials is of interest, to study the recombination dynamic of the charge carriers in perovskite materials.

1.3.1 Incoherent cathodoluminescence

The mechanism of incoherent emission is highly similar to that of photoluminescence, mainly recombination of electron-hole pairs in the sample. The sample is first excited and then decays inelastically by emitting light. The difference between photoluminescence and cathodoluminescence is the mode of excitation. Photoluminescence is excited by photons which preferentially couple to strong-dipole modes, whereas cathodoluminescence is excited by electrons which transfer large momenta to the sample and enhance the probability of nondipole transitions. Furthermore, the excitation electrons in our system (1 – 10 keV) carry much higher energy, hence able to excite large-band-gap insulator.

Recombination emission

Recombination emission is the dominant process in a semiconductor upon electron bombardment. Under electron beam, a material absorbs the energy of electron beam. An electron which was originally in valence band (ground state) is excited to high energy states, leaving a vacancy (hole) in valence band. Upon a molecule being excited to any higher electronic states, the electronic states depend on the excitation energy. However, emission wavelength observed from the molecule does not depend on the excitation

wavelength. This is because Kasha's rule states that photon emission that occurs in significant yield only results from the transition from the lowest excited states of a given multiplicity. This can be explained by the Franck-Condon principle which states that an electronic transition from one vibrational energy level to another will occur more likely if the two vibrational wave functions overlap more significantly. The overlap of vibrational wavefunctions is the greatest between the two energy levels that are close to each other. In most molecules, high energy levels lie closely together, hence the molecules in upper states reach the lowest excited states quickly, before they release photons [22]. After inter-band relaxation process, the relaxation of electron to the ground state causes recombination of electrons and holes, with release of a photon. This emission is dominant in semiconductors and insulators but impossible to be emitted from metals because there is no band gap in metals.

For recombination emission, cathodoluminescence signals are usually distinguished into intrinsic and extrinsic luminescence. Intrinsic luminescence results from band-to-band transition, photon is emitted with energy $hv = E_g = E_c - E_v$, whose energy level is illustrated in Figure 1-2a. Extrinsic luminescence results from the transition of energy states within the band gap. Impurities or lattice defect can trap electrons or holes at the energy states within the forbidden gap. Recombination of an electron and a trapped hole releases a photon (Figure 1-2b). A trapped electron may be excited to the conduction band then recombine with an acceptor, this results in emission of a photon (Figure 1-2c). Another case is the trapped electron may relax to the ground state after certain time (Figure 1-2d) or some other activator levels due to the defects of material (Figure 1-2e) and emit a photon. The excitation and relaxation between the energy states within the forbidden gap is also possible (Figure 1-2f) [19].

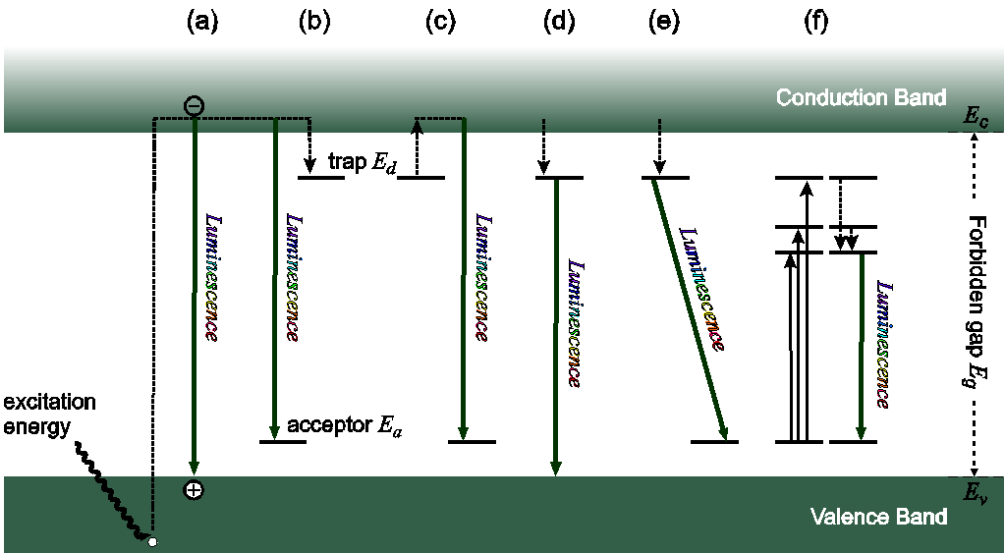

Figure 1-2. Mechanisms of generation of CL response in an insulator or semiconductor, as conceptualized with band theory [19].

1.3.2 Coherent electron induced emission

Coherent electron induced emission is induced through several mechanisms such as Cherenkov radiation, transition radiation and Bremsstrahlung radiation. The sources of these coherent emission have relatively delocalized origin since they involve large regions from electronic point of view [9]. High electron energy increases the coherent photon yield because faster electrons carry more extended external field and coupling to delocalized excitations more efficiently.

Calculation of coherent light emission

The information of electron-beam-induced light emission can be obtained by solving the Maxwell's equations using boundary element method (BEM), which was performed by F. J. García de Abajo and A. Howie [5,6]. An incident electron with electromagnetic field $\boldsymbol{E_{ext}}$ and $\boldsymbol{H_{ext}}$ will induced another electromagnetic fields, $\boldsymbol{E_{ind}}$ and $\boldsymbol{H_{ind}}$.

Starting from Maxwell's equation:

$$\nabla \cdot \boldsymbol{D} = 4\pi\rho, \qquad \nabla \times \boldsymbol{H} + ik\boldsymbol{D} = \frac{4\pi}{c} j \tag{1.9}$$

$$\nabla \cdot \boldsymbol{B} = 0, \qquad \nabla \times \boldsymbol{E} - ik\boldsymbol{B} = 0 \tag{1.10}$$

where $k = \omega/c$, ρ is the charge density, j is the current density, $\boldsymbol{D}$ is the electric displacement and $\boldsymbol{B}$ is the magnetic induction, such that:

$$\boldsymbol{D} = \varepsilon \boldsymbol{E}, \qquad \boldsymbol{B} = \mu \boldsymbol{H} \tag{1.11}$$

where ε is dielectric constant and μ is magnetic permeability of the specimen.

Expressing equations (1.9) and (1.10) in terms of scalar potential φ and vector potential $\boldsymbol{A}$:

$$\boldsymbol{E} = ik\boldsymbol{A} - \nabla\varphi \tag{1.12}$$

$$\boldsymbol{H} = \frac{1}{\mu}\nabla \times \boldsymbol{A} \tag{1.13}$$

Working in the Lorentz gauge ($\nabla \cdot \boldsymbol{A} = ik\varepsilon\varphi$), the potentials become:

$$\varphi = \varphi_{ext} + \int_{S_j} d\boldsymbol{s} G_j(|\boldsymbol{r} - \boldsymbol{s}|)\sigma_j(s) \tag{1.14}$$

$$\boldsymbol{A} = A_{ext} + \int_{S_j} d\boldsymbol{s} G_j(|\boldsymbol{r} - \boldsymbol{s}|)\boldsymbol{h_j}(s) \tag{1.15}$$

where r is the coordinate vector inside the medium, s is the coordinate vector running over the interfaces, σ_j and $\boldsymbol{h_j}$ the auxiliary interface charges and currents in medium j.

G_j is the Green's function of the Helmholtz equation inside medium j:

$$G_j = \frac{exp(ikr\sqrt{\varepsilon_j})}{r} \tag{1.16}$$

The induced electric and magnetic field at $\boldsymbol{r}$ can be determined by using BEM to solve Maxwell's equations. Next, consider the radiated energy by integrating the Poynting vector which is perpendicular to the large virtual sphere around the object over the whole sphere and over time.

$$\Delta E_{rad} = \frac{c}{4\pi} \int dt \int d\,\Omega_r \cdot r^2 (\boldsymbol{E_{ind}} \times \boldsymbol{H_{ind}}) \cdot \boldsymbol{r} \tag{1.17}$$

where $\boldsymbol{r}$ is the pointing radially outwards and Ω_r is the solid angle [9]. In term of frequency, equation (1.17) becomes:

$$\Delta E_{rad} = \int_0^\infty \omega d\omega \int d\,\Omega_r \cdot \Gamma_{rad}(\omega, \Omega_r) \tag{1.18}$$

and

$$\Gamma_{rad}(\omega, \Omega_r) = \frac{cr^2}{4\pi^2 \omega} Re[(\boldsymbol{E_{ind}} \times \boldsymbol{H_{ind}}) \cdot \boldsymbol{r}] \tag{1.19}$$

where Γ_{rad} is the probability of the system emitting a photon with energy $\hbar\omega$ per solid angle. Note that this electron-induced coherent radiation emission is dominant at relatively high electron-beam energies (above 10 keV), it decays and be overcome by incoherent cathodoluminescence at low electron energy [9].

Transition radiation

Transition radiation is also emitted when an electron passes form one medium to another. When an electron from the first medium incident onto the surface of the second medium, a perturbation in the electrons of second medium and polarization charge is created. The incoming electron and the induced charge act as induced dipole. Once the electron crosses the interface, the effective dipole is annihilated, generating emission in far field, namely transition radiation [25].

Cherenkov radiation

Cherenkov radiation is emitted when an electron travels faster than light in a medium:

$$v > \frac{c}{n(\lambda)} \tag{1.20}$$

where v is the speed of the electron, c is the speed of light and $n(\lambda)$ is the refractive index of the medium with respect to wavelength.

Incoming electrons disrupt the local electromagnetic field in a medium and induce radiation (photons) in the medium. If the speed of the electrons is slower than the speed of light in the medium, photons interfere destructively. On the other hand, if the speed of the electrons is higher than the speed of light in medium, the energy radiates constructively as a coherent shockwave, resulting in emission of photons [26]. Cherenkov radiation can only be observed when the velocity of electrons is high enough (accelerating voltage of at least 50 keV).

Bremsstrahlung radiation

Bremsstrahlung radiation, which is also known as braking radiation, is the electromagnetic radiation emitted when there is a sudden change in a charged particle's trajectory. An incident electron charge particle is deflected by a heavy atomic nucleus and decelerate. The kinetic energy lost by the incident electron is compensated by emission of a photon. Since our system deals with 1 keV to 10 keV electron energy, the energy of bremsstrahlung photons is in X-ray range. Besides that, the spectrum of bremsstrahlung radiation is continuous due to different impact parameters for each interaction.

Main Source of Observable Radiation from Perovskites

Knowing the source of signals obtained is very important in data analysis. Different photon-emission processes are induced by electron bombardment. Some mechanisms mentioned in previous sections can be selectively eliminated, depending on the properties of target materials, the range of data acquisition and experiment parameter values. Firstly, Cherenkov radiation can be excluded because Cherenkov radiation can only be observed when the velocity of electrons is higher than velocity of light in materials (accelerating voltage of at least 50 keV). This is hardly observed in our system which operates at maximum 10 keV. Next, the generation of surface plasmons occurs only at the interface of two media whose real part of permittivity are in opposite sign, such as dielectric-metal interfaces (dielectric with positive permittivity whereas metals with negative permittivity). Over the last decades, cathodoluminescence technique has been used to study plasmons excitation in metals [9]. In fact, surface plasmons can hardly be generated at semiconductor. Another notable point is transition radiation is an unavoidable electromagnetic radiation emitted when an electron crosses the interface of two media with different dielectric constants. This is the reason why the background CL signal is never zero but always broad and low magnitude order.

In the case of many semiconductors and dielectrics, especially in strongly luminescent materials like perovskites, incoherent luminescence (from e-h pair recombination) is the main source of radiation as it is usually orders of magnitude stronger than transition radiation. Brenny et al. also reported that transition radiation increases with increasing accelerating voltage applied because higher energy electrons have electric fields that extend further from its trajectory, hence polarize larger volume of materials and induce more surface currents [27]. Nevertheless, cathodoluminescence signals should be corrected by subtracting transition radiation which can be calculated based on the

theoretical formalism described in section IV-C of Ref. [9], especially when high accelerating voltage is used.

It is also worth mentioning that high energy photons (X-rays) are also emitted upon electron bombardment. A characteristic X-ray photon is emitted during the transition of an electron from outer shell to inner shell, in order to fill up the vacancy left behind by an inner electron being kicked out by high energy incident electron. Bremsstrahlung radiation, which is also known as braking radiation, is emitted when there is sudden change in incident electron trajectory. Since electron microscopy deal with electrons of 1-10 keV, the energy of Bremsstrahlung photons is in X-ray range in our system. These X-ray photons can be excluded in our case because they are not in our acquisition range (UV-Visible range).

1.4 Cathodoluminescence Technique

1.4.1 Excitation system

Traditional TRCL setup equipped a beam-blanking unit below the electron gun of SEM to generate electron pulses (Figure 1-3) [12,13]. The beam-blanking unit is driven with a generic electrostatic pulse generator which also synchronize to the time-related photon counting detector. Due to the long duration of the electron pulse generated by beam-blanking mechanism ($> 1\ ns$), the time resolution ($< 200\ ps$) of the traditional TRCL system is limited by the resistivity relative to beam current density, the speed of deflecting the electron beam and the blanking time [30]. Shorter electron pulse duration is required to study the characteristic relaxation time in semiconductors. Besides that, when the beam is blanking, the beam pointing shall be shifted by few micrometres away, even if picosecond blanking speed is achieved, the space-resolution of the system is

ruined. Moreover, most of the beam current will be lost after being chopped. One of the simplest means of obtaining shorter electron pulse is to use laser-triggered electron sources. By illuminating a photoemission-based electron gun with a short pulse laser of energy above the work function of the material of the electron gun, a very short pulse of electrons which has approximately the same duration as the laser pulse can be created. This approach has removed the limitation of the detector as a factor of limiting temporal resolution and makes the "source laser" the major determining factor for temporal resolution. This approach requires drastic modification of SEM and low effective current in the pulsed beam, the signal to noise ratio of the images.

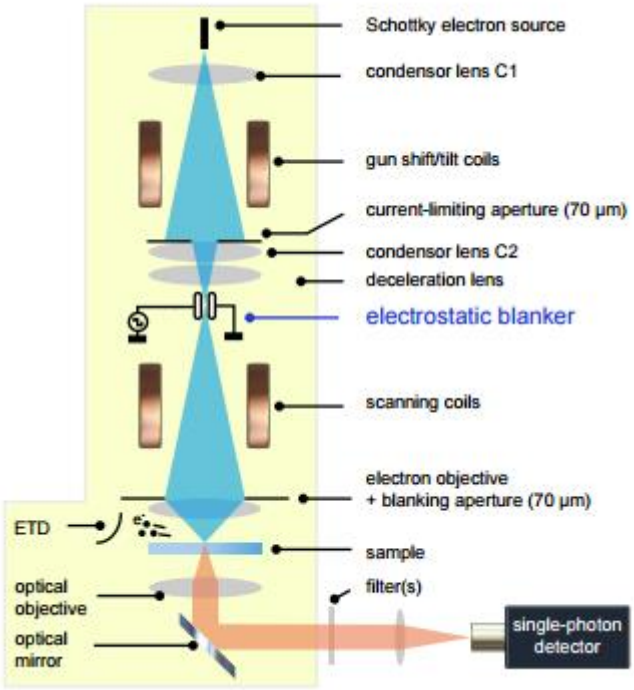

Figure 1-3. Experimental setup to measure time-resolved CL by installing electrostatic beam blanker [31].

The system at SPMS uses a high brightness photoelectron gun which can generate high beam current to ensure that there is still enough current within the electron spot to record secondary electron images, and a picosecond laser to drive the photoelectron gun. Picosecond laser sources are more economical than femtosecond lasers and sufficient to observe the luminescence decay of materials. It is important to note that after the short electron pulses are generated, coulomb repulsion between the charged particles in an electron packet will result in space charged induced transverse and longitudinal expansion of the packet [32]. Longitudinal broadening directly influence the temporal length and energy spread of the electron packet, and consequently the temporal resolution of the time-resolved system [33].

1.4.2 Detection system

Figure 1-4 offers an overview of the time and length scales of different dynamic processes. The dynamic process of interest is electronic process, atomic, molecular and lattice dynamics, with time scale from picoseconds to attoseconds. The time resolution of a system is often affected by the performance of detector besides electron pulse length. In the system at SPMS, time resolved detection is achieved by using Optronis Optoscope SC-10 streak camera is used to collect photons emitted at range 200-850 nm, with intrinsic temporal resolution >2ps. A streak camera converts temporal information into spatial information by applying time-varying electric field.

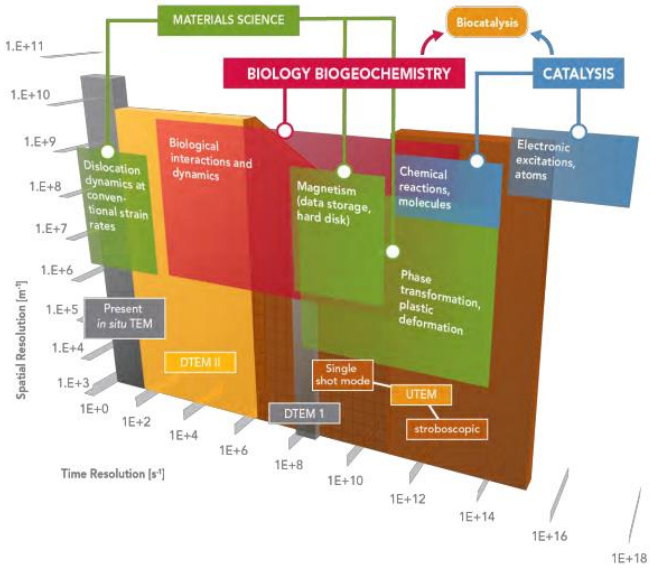

Figure 1-4. Overview of the time scales and length scales of different dynamic processes [34].

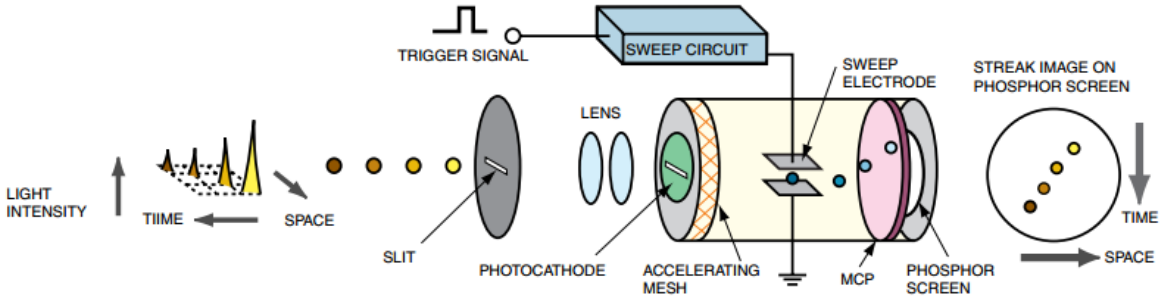

Figure 1-5. Operating principle of a streak camera [35].

Figure 1-5 shows the operating principle of a streak camera. The luminescence signals collected are firstly converted into electron pulses by the photocathode. Next, the electron pulses are deviated by deflection plates which apply time-varying electric field with same frequency of the pulsed laser repetition rate to synchronize the signal. The deviated electrons are amplified by multichannel plate (MCP) and then converted back into photons by the phosphor screen.

The time resolution of streak camera is affected by the aperture of temporal slit and the speed of the trigger jitter. The temporal slit should be as small as possible and the trigger jitter should be as fast as possible.

1.4.3 Time resolution of TRCL

The temporal resolution of a system can be obtained by deconvolving the TRCL signal with the time-resolved photoluminescence (TRPL) from a GaAs:Si sample. This method is inconvenient because both TRPL signal should be obtained under same experimental configuration as TRCL. Instead, the time resolution of TRCL system can obtained with direct fitting and analysis of the TRCL data [36].

The carrier population evolution excited by an electron pulse can be expressed in the equation below:

$$\frac{dN}{dt} = f(t) - \frac{N}{\tau_r} - \frac{N}{\tau_{nr}} \tag{1.21}$$

where $f(t)$ is the electron pulse profile, N is the number of carriers at time t, τ_r is the radiative carrier lifetime and τ_{nr} is the non-radiative carrier lifetime. The number of photons generated at time t is assumed have proportional relationship with $N(t)$.

By integrating equation (1.21),

$$N(t) = exp(-\frac{t}{\tau}) \int_0^t f(x) \cdot exp\left(\frac{x}{\tau}\right) \cdot dx \tag{1.22}$$

where

$$\frac{1}{\tau} = \frac{1}{\tau_r} - \frac{1}{\tau_{nr}} \tag{1.23}$$

Now, by assuming that $N_0 = N(t = 0) = 0$ and the electron pulse profile is Gaussian as expressed in equation (1.24), the experimental data can be fitted with equation (1.25). The duration of the electron pulse can be obtained by calculating the FWHM of the Gaussian profile as stated in equation (1.26) by using the value of parameter σ. This is the temporal resolution of the TRCL setup. Better fitting can be done by considering two-channel decay (bi-exponential fitting).

$$f(x) = \frac{1}{\sigma\sqrt{2\pi}} exp(-\frac{1}{2}\left(\frac{x-\mu}{\sigma}\right)^2 \tag{1.24}$$

$$N(t) = N_0 \cdot exp(-\frac{t}{\tau}) \int_0^t \frac{1}{\sigma\sqrt{2\pi}} exp[-\frac{(x-x_0)^2}{2\sigma^2}] \cdot exp\left(\frac{x}{\tau}\right) \cdot dx \tag{1.25}$$

$$FWHM = 2\sqrt{2\,ln\,2}\,\sigma \tag{1.26}$$

Future Development of TRCL resolution

The temporal resolution is presently limited by the repulsion between the electrons inside the pulse, causing electrons with different initial velocities arrive at the sample earlier or later, consequently develop temporal broadening during propagation. It is however possible to be overcome. In the Physical Biology Centre for Ultrafast Science and Technology (UST) at Caltech, Ultrafast Electron Microscopy (UEM) that makes the direct imaging of the ultrafast dynamic process in short timescale has been developed by Zewail et al. [37]–[39]. Figure 1-6 shows UEM imaging of a single protein vesicle, obtained at different time [40].

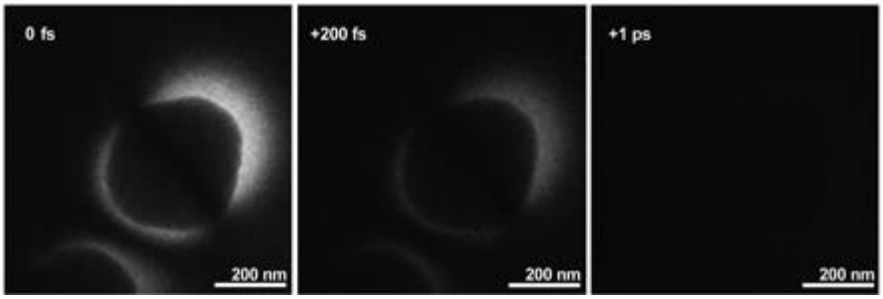

Figure 1-6. UEM imaging of a single protein vesicle at 0 fs, +200 fs and +1 ps [40].

Much higher resolution (up to femtosecond) resolution is achievable in UEM with single-electron coherent packets [41]. Single-electron coherent packet describes the case when each timed electron packets contain a small number of electrons such that the Coulombic repulsion is insignificant. In short, single-electron coherent packets can avoid electron repulsion, allowing shorter electron pulse duration hence higher spatiotemporal resolution. Aidelsbrurger et al. reported that the electron packets can contain, with highest probability, single electrons by properly adjusting the energy of the femtosecond laser pulse [42]. Hommelhoff et al. reported that electron pulse durations of 1 fs is achievable through single electron generation by 8 fs laser pulses [43]. Such high time resolution will allow investigation on more dynamics processes that happen at shorter time scale. Spatial resolution will also be improved if the single-electron packet excitation is installed.

Chapter 2

Perovskite Materials

2.1 Properties of Perovskite

2.1.1 Structure of Perovskite

In 1839, Calcium Titanium Oxide ($CaTiO_3$) mineral was discovered by Gustav Rose from rock samples found in Ural Mountains, Russia and Kazakhstan. It was named "Perovskite", after the name of a Russian mineralogist, Count Lev Aleksevich von Perovski [44]. Soon, the perovskite crystal structure was introduced by Victor Goldschmidt in 1926, when he was working on tolerance factors [45]. Perovskite became a name to the class of compounds which have the crystal structure ABX_3, the same type of crystal structure as $CaTiO_3$.

The general chemical formula of the perovskite structure is ABX_3, "A" and "B" are cations whereas "X" is anion, often oxygen or halogen. In the case of halide perovskites (X = halogen) B is usually a divalent cation of the group IV elements (e.g. Ge^{2+}, Sn^{2+}, Pb^{2+}) but it can also include transition metals (e.g. Cu^{2+}, Ni^{2+}) and alkaline earth metals (e.g. Sr^{2+}, Ba^{2+}). A is a monovalent cation which can be inorganic (e.g Cs+, Rb+) or organic (methylammonium, formamidinium). The unit cell of the ideal perovskite structure is shown as the cubic in Figure 2-1. Its respective atomic coordinates are shown in Table 2-1. Cations A, which are usually larger than cation B in size, are located at the corner of the cube. Cation B is located at the center of the cube, and is in octahedral coordination with X, which therefore collocate at the face-centered positions. Cation A occupies the cuboctahedral cavities keeping the electroneutrality of the system. The

repetition of the unit cell along the 3 dimensions creates then the perovskite crystal lattice.

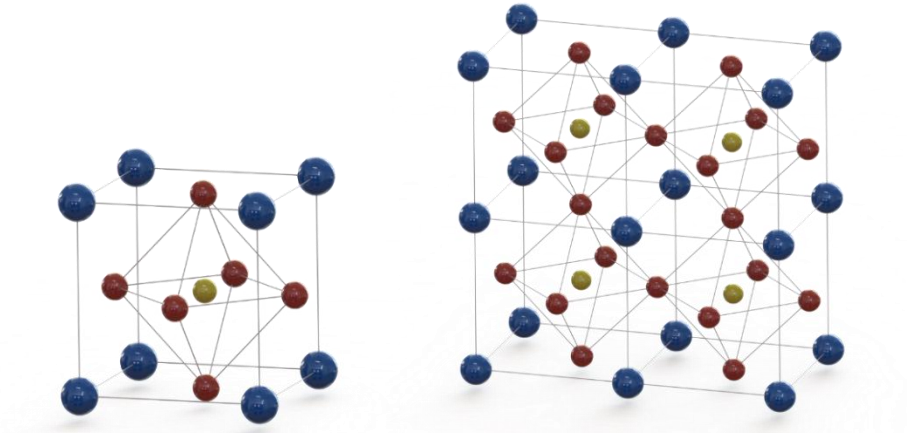

Figure 2-1. (a) Ideal atomic structure and (b) more complex crystal structure of perovskite. (illustration by author)

Table 2-1. The atomic co-ordinations of perovskite structure.

Atom	Co-ordinates	Coordination number	Geometry
A	$(0,0,0)$	12	Cuboctahedron
B	$\left(\frac{1}{2},\frac{1}{2},\frac{1}{2}\right)$	6	Octahedral
X	$\left(\frac{1}{2},0,0\right),\left(0,\frac{1}{2},0\right),\left(0,0,\frac{1}{2}\right)$	6	Octahedral

Note that Strontium Titanate ($SrTiO_3$), Strontium Stannate ($SrSnO_3$) and Barium Zirconate ($BaZrO_3$) have ideal perovskite structure (cubic), however, most of natural perovskites, such as $CaTiO_3$, Calcium Metastannate ($CaSnO_3$) and Calcium Zirconate ($CaZrO_3$), are determined to be orthorhombic ($a \neq b \neq c$) perovskite instead of cubic by Helen D Megaw using X-ray powder photographs [46]. Besides cubic and orthorhombic, there exist other forms of perovskite structures such as tetragonal and rhombohedral [46]. There are hundreds of material adopting perovskite structure, with

huge variation of characteristics such as semiconducting, insulating, piezoelectricity and superconducting [30,31]. In 1990s, halide perovskite was found to have the electricity-to-light conversion ability by Mitzi's group [32,33]. Almost two decades later, in 2006, in order to find an absorber which allows high light absorption in thin film, a perovskite compound which worked as visible light sensitizer in a photochemical cell was reported by T. Miyasaka and his team [51]. Since then, hybrid halide perovskites have drawn much attention as absorbers for solar cells due to their light-to-electricity (photovoltaic) conversion.

2.1.2 Organic-inorganic hybrid perovskites

Organic-inorganic hybrid perovskites open an interesting path to the field of photophysics. Inorganic materials usually have high mechanical hardness (since they form ionic bonds), high electron mobility and some magnetic properties, however, their fabrication cost is high. Layers of organic compounds, on the other hand, can be fabricated in low cost by simple procedures such as spin-coating. Organic compounds also have beneficial properties such as polarizability and high flexibility but weak interactions between molecules. Organic-inorganic hybrid material has shown the possibility to combine the properties of organic component and the inorganic component, resulting in having marvellous characteristics. The versatility of the perovskite structure allows to obtain materials with mixed cations and halides, leading to the fine tuning of their optical properties; examples of this are $MAPbI_{3-x}Cl_x$ [28,29], $MAPb(I_{1-x}Br_x)_3$ [54], $FAPbI_yBr_{3-y}$ [55], $FAPbI_{3-x}Cl_x$ [56] and $(FAPbI_3)_{0.85}(MAPbBr_3)_{0.15}$ [57]. Organic-inorganic perovskite materials have been reported to have long carrier diffusion length [5], [58], [59]. The average distance travelled by the charge carriers before recombination is long. This is mainly due to the low exciton binding energy of

perovskite materials [60]. This indicates that free charges are predominantly generated and tend to have long recombination lifetime.

2.1.3 Crystallographic phases and respective structure of perovskites

In early 1920, Goldschmidt introduces tolerance factor [45]. Goldschmidt's tolerance factor, τ, is an indicator for the stability of a 3D perovskite lattice ABX_3 and the degree of distortion of crystal structure. It is the ratio of the distance between A and X to the distance between B and X, as shown in equation (2.1).

$$Tolerance\ factor, \tau = \frac{R_A + R_X}{\sqrt{2}(R_B + R_X)} \tag{2.1}$$

R_A, R_B, R_X correspond to the atomic radius of A, B and X respectively. There are 4 different phases of perovskite structure under different conditions. Under ideal conditions, tolerance factor, τ, lies between 0.89 and 1 [61], and the perovskite has cubic structure and in α phase. In order to satisfy $\tau \sim 1$, the atomic radius of A should be larger than B. The tolerance factor is different at different range of temperature due to the change in the structure. For most of the perovskite, the tolerance factor becomes in range 0.71 to 0.89 when temperature decreases, the structure of the perovskite is no longer cubic, it becomes lower symmetry tetragonal (β phase) or orthorhombic (γ phase) structure, with unit cell ($\sqrt{2} \times \sqrt{2} \times 2$), based on α phase [62]. δ phase is the structure much deviated from the ideal perovskite structure, it was found for certain perovskite such as Cesium Lead Iodide ($CsPbI_3$), Formamidinium Lead Iodide ($FAPbI_3$) and Cesium Tin Tri-iodide ($CsSnI_3$) [63]. When the organic cation A is too big compared to the central cation B, it will not fit inside the cuboctahedral cavities of the 3D perovskite, and there will be a rearrangement into a two-dimensional perovskite with general formula $(NH_3 - R - NH_3)MX_4$. Such structures are characterized by an alternation of organic and inorganic sheets. Perovskite sheets can be imagined as

deriving from the cut along certain direction of the 3D perovskite lattice. The orientation of the perovskite sheets is affected by the choice of organic cation [50]. The degree of interaction within the perovskite may be decided by the organic cation [64]. Table 2-2 summarizes the tolerance factor and the structure of perovskite.

The transitions between different phases occur at specific temperatures [65]. Organic-inorganic perovskites have more complicated atomic structure compared to inorganic perovskite because they have more possible orientations of the cations, which can also result in a polarization of the structure upon application of electrical bias. In organic-inorganic perovskites, the organic molecules are orientated randomly at α phase but have less freedom in β phase. At low temperature (γ phase), organic molecules are frozen and their alignments are fixed [65].

Table 2-2. The structures of perovskite at respective tolerance factor.

Tolerance factor, τ	**Phase**	**Structure**	**Ionic radii**
>1	-	Hexagonal	A ion >> B ion
0.89-1.00	α	Cubic	A ion > B ion (ideal ratio)
0.71-0.89	β, γ	Tetragonal/ Orthorhombic	A ion is not large enough to fit into the interstices of B ions
<0.71	δ	Different structures	A ion ≈ B ion

Since the different phases have different bandgaps, cathodoluminescence could be used as an effective tool to differentiate among them across the phase diagram by varying temperature.

2.2 Materials studied

This project starts with $MAPbI_3$ and $CsPbBr_3$ perovskites which have been widely studied, to first deal with the issue of stability of materials and resolution of signals, also as a calibration for our CL system. One of the main reason of choosing these materials is their bandgaps lie in the visible range ($1.65\,eV$ to $2.75\,eV$). This property is especially important for applications such as solar cells and light emitting diodes (LED). The lead halide perovskites $MAPbI_3$ has proven to be an exceptional light harvester for hybrid organic-inorganic solar cells [66]. Inorganic lead halide perovskite $CsPbBr_3$ is also studied because of its exceptional luminescence and band gap in visible range.

Next, a hybrid perovskite of Ruddlesden-Popper series, with chemical formula $(PEA)_2(MA)_{n-1}$ $[Pb_nI_{3n+1}]$, was studied. Hybrid perovskites with Ruddlesden-Popper series consists of stacks of alternating organic and inorganic layers whose thickness can be controlled by reaction stoichiometry. Different heterogeneous domains are found during the formation of this perovskite film. Cathodoluminescence is the ideal equipment to investigate the spatial distribution of self-organized heterogeneous domains in this perovskites film, in the aspect of its luminescence properties and recombination dynamics.

2.2.1 Properties of $MAPbI_3$

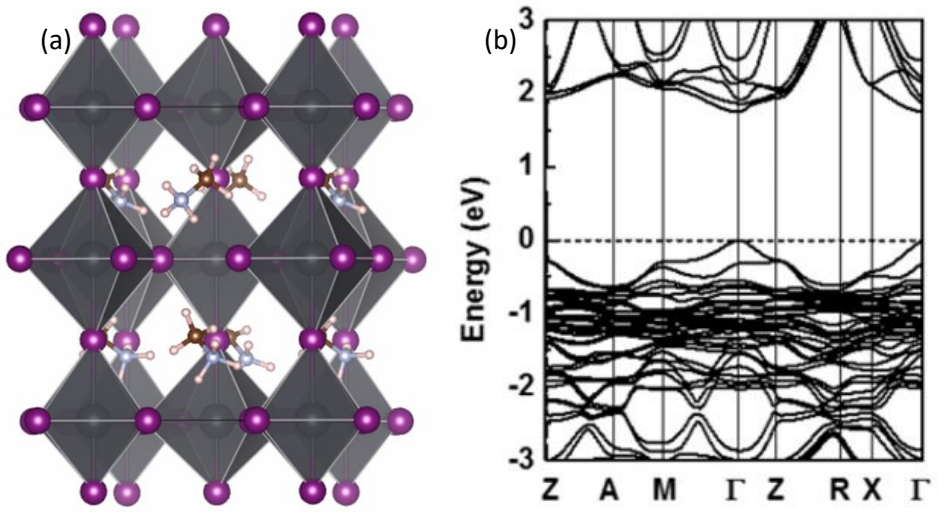

Figure 2-2. (a) The structure of $MAPbI_3$. Purple ions represent iodide, the ions surrounded by iodide are lead, blue ions represent oxygen, brown ions represent carbon and white ions represent hydrogen. (b) Band structure of $MAPbI_3$ [67].

Figure 2-2a shows the structure of methylammounium lead iodide $CH_3NH_3PbI_3(MAPbI_3)$. Note that the basic electronic structure and the total energy of $MAPbI_3$ have insignificant dependence on the orientation of methylammonium ion, $CH_3NH_3^+$ (MA) because it lies in an isotropic cage made of iodide anions, where methylammonium can assume various orientation. Here the positive ammonium moieties can interact equally with every negatively charged iodide ion by coulombic attraction [68]. Figure 2-2b shows the band structure of $MAPbI_3$ calculated by J. Yin et al. in our group based on van der Waals density functional (vdW-DF2) [67]. It shows a direct band gap energy $E_g \approx 1.60\ eV$ at Γ point. The transition temperatures of $MAPbI_3$ between α phase (cubic), β phase (tetragonal) and γ phase (orthorhombic) are summarized in Table 2-3 [65]. When the temperature decreases down to certain value, cubic phase is transformed into tetragonal phase, then transformed into orthorhombic phase when temperature further decreases because of the ordering of MA ions. $MAPbI_3$ adopts tetragonal crystal system, space group *I4/mcm* and lattice parameters a = 8.87 Å,

c = 12.65 Å at room temperature [69]. The three-dimensional crystal structures of $MAPbI_3$ at cubic phase, tetragonal phase and orthorhombic phase are shown in Figure 2-3.

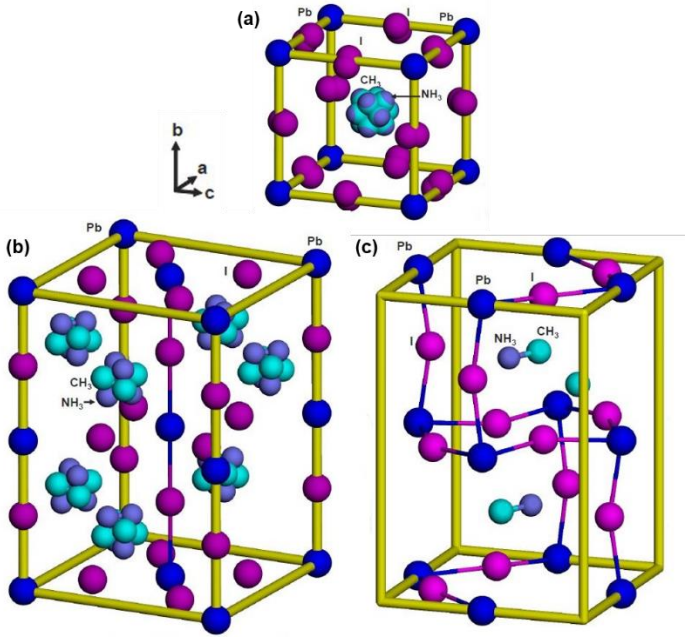

Figure 2-3. Structural model of $MAPbI_3$ with (a) cubic, (b) tetragonal and (c) orthorhombic structures [70].

Table 2-3. Transition temperature of $MAPbI_3$ summarized from references [71][72][73].

	$MAPbI_3$
Crystal system / Phase	Cubic / α
Transition temperature (K)	330
Crystal system / Phase	Tetragonal / β
Transition temperature (K)	161
Crystal system / Phase	Orthorhombic / γ

2.2.2 Properties of $CsPbBr_3$

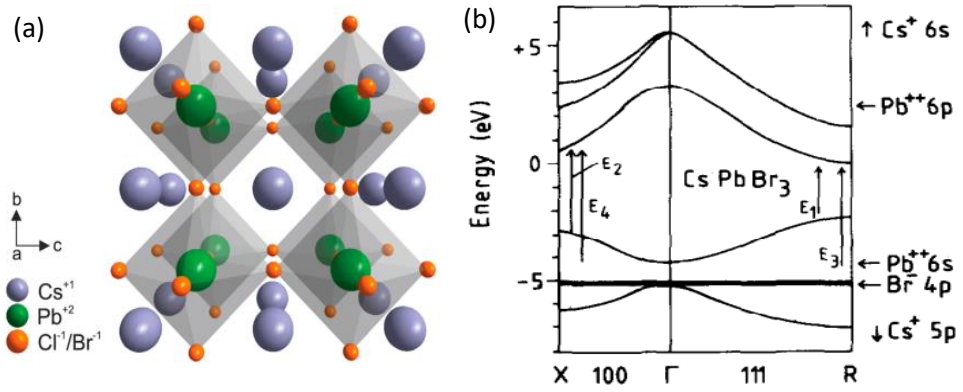

Figure 2-4. (a) The crystal structure [74] and (b) band structure of $CsPbBr_3$ [75].

Inorganic perovskite $CsPbBr_3$ is investigated because inorganic ion Cs^+ shows less volatility, hence with higher stability. The degradation due to heat and humidity can be significantly reduced [76]. Its stability under high energy electron beam might be higher than organic-inorganic perovskites. The crystal structure of $CsPbBr_3$ (Figure 2-4a) has been previously reported in literatures [57]. Heidrich developed a model based on an empirical linear combination of atomic orbitals (LCAO) [75]. It shows that $CsPbBr_3$ has a direct band gap energy $E_g \approx 2.20\,eV$ at R point at room temperature. The transition temperatures of $MAPbI_3$ between α phase (cubic), β phase (tetragonal) and γ phase (orthorhombic) were studied by Stoumpos et al and their results are summarized in Table 2-4 [78]. When temperature goes down to 403K, the cubic phase is transformed into tetragonal phase, then transformed into orthorhombic phase at 361K.

Table 2-4. Transition temperatures of $CsPbBr_3$ [78].

	$CsPbBr_3$
Crystal system / Phase	Cubic / α
Transition temperature (K)	403
Crystal system / Phase	Tetragonal / β
Transition temperature (K)	361
Crystal system / Phase	Orthorhombic / γ

2.2.3 Properties of $(PEA)_2(MA)_{n-1}\,[Pb_nI_{3n+1}]$ (two-dimensional perovskite)

As mentioned in section 2.1.3, two-dimensional perovskite will be formed when the organic cation A is much larger than cation B. We hereby introduce a bulky cation, phenylethylammonium ($PEA = C_8H_9NH_3$) into $MAPbI_3$ to induce the formation of layered perovskites of the Ruddlesden-Popper series with chemical form $(PEA)_2(MA)_{n-1}\,[Pb_nI_{3n+1}]$. Figure 2-5a shows its structures with different n values. For n = 1, the perovskite is $(PEA)_2PbI_4$, in a pure 2-dimensional structure. For n = 2, the perovskite is $(PEA)_2(MA)\,[Pb_2I_7]$, in a quasi-2D dimensional structure (intermediate between 2D and 3D). For n = ∞, the perovskite structure can be simplified to the 3-dimensional perovskite. The band gap of the perovskite with different n values is different. Suppose a film of perovskite with different n values is synthesized, the carriers can be directed to the smallest bandgap region and concentrated at the region, hence increase the emission efficiency, as illustrated in Figure 2-5b. By adjusting the ratio of PEA iodide to methylammonium iodide (MAI), grains with composition $(PEA)_2(MA)_{n-1}\,[Pb_nI_{3n+1}]$, with average grain comprising $\langle n \rangle$ layers of PbI_6 is produced.

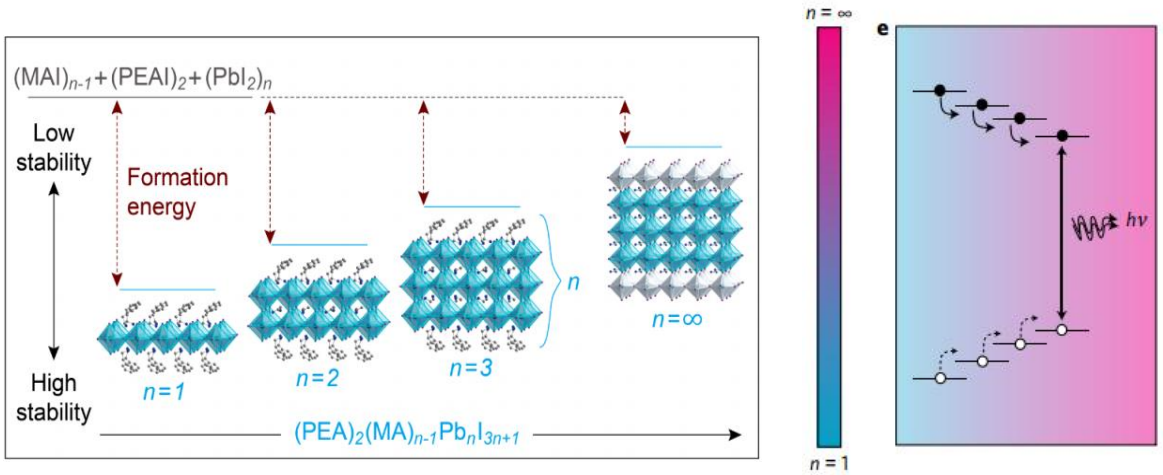

Figure 2-5. (a) Unit cell structures of $(PEA)_2(MA)_{n-1}\,[Pb_nI_{3n+1}]$ with different n values [79]. (b) Energy funnelling of multi-phase perovskite materials $(PEA)_2(MA)_{n-1}\,[Pb_nI_{3n+1}]$ [80].

2.3 Syntheses of perovskites

2.3.1 Synthesis of $MAPbI_3$

74.4 mg of MAI was mixed with 57.7 mg of lead(II) acetate trihydrate (1:1 atomic ratio) in 500 μl of DMF solvent. The solution was heated on a hotplate at 100 °C.

$$Pb(Ac)_2 \cdot 3H_2O + 3CH_3NH_3I \rightarrow MAPbI_3 + 2MA^+ + 2Ac^+ + 3H_2O$$

35 μl of the solution was drop casted on the substrate then spun at 5000 rpm for 30 seconds using spin coater, then annealed at 100 °C for 15 minutes to evaporate the solvent, the excess of organics Ac^+ and MA^+ and the water byproduct. After the end of the spin coating, the film remains colourless, and only turns dark purple upon annealing; a change that marks the perovskite formation. The procedures are summarized in Figure 2-6. The spin coater used is installed in a glove box to allow the spin coating in an inert atmosphere and have complete control over the crystallization conditions.

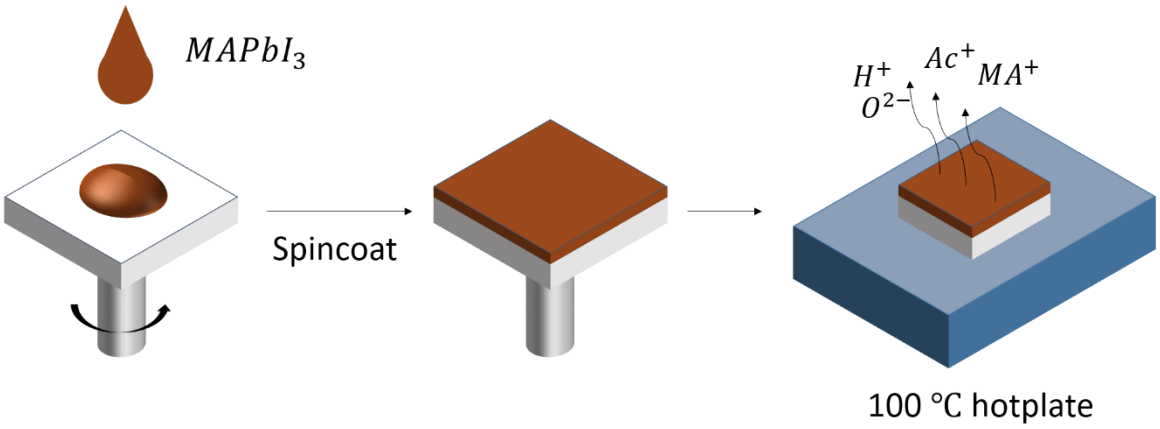

Figure 2-6. Procedures for fabrication of $MAPbI_3$ film.

2.3.2 Synthesis of $CsPbBr_3$

The sysnthesis of $CsPbBr_3$ was adapted from the synthetic method reported by D. Zhang *et al*. [81] and Protesescu *et al.*[82]. Firstly, 0.4 g Cs_2CO_3 and 1.2 ml of oleic acid (OA) were loaded into a 3-neck flask while 15 ml of octadecene (ODE) is degassed and dried under vacuum at 120 °C for 1h. The solution was then heated at 150 °C under nitrogen gas until all Cs_2CO_3 dissolves to form Cs-oleate solution. Next, 5 ml of ODE and 0.069 g of $PbBr_2$ were loaded into another 3-neck flask and degassed under vacuum at 120 °C for 1h. 0.3 ml of oleyamide (OLA) and 0.4 ml OA were injected into the flask at 120 °C under nitrogen. The temperature was then increased to 200 °C for 1h. Next, 0.6 ml of Cs-oleate solution was injected rapidly. After 8 minutes, the mixture was cooled in ice-water bath.

2.3.3 Synthesis of $(PEA)_2(MA)_{n-1}$ $[Pb_nI_{3n+1}]$

In this work, two thin films and three single crystals are synthesized. The thin films include pure 2D perovskite $(PEA)_2PbI_4$ and heterogeneous films formed by mixed phases of quasi-2D perovskite of series $(PEA)_2(MA)_{n-1}$ $[Pb_nI_{3n+1}]$. Pure n = 1, n = 2 and n = ∞ single crystals were also synthesized by adapting the synthetic strategy reported by C. C. Stoumpos *et al.* [83] for similar multidimensional perovskites.

For the synthesis, the following chemicals were used: phenethylammonium iodide $(PEA)I$ (Dyesol), lead iodide PbI_2 (99.99%, TCI), methylammonium iodide MAI (Dyesol), methylammonium chloride $MACl$ (Dyesol), stabilized hydroiodic acid HI (Sigma Aldrich), 50% aqueous H_3PO_2 (Sigma Aldrich), lead oxide PbO (Sigma Aldrich), phenethylamine (Sigma Aldrich), g-butyrolactone GBL (Sigma Aldrich), N,N-dimethyl sulfoxide DMSO (98%, Sigma Aldrich).

A. Synthesis of $(PEA)_2\ PbI_4$ single crystal (n = 1)

2 mmol of PbO powder was dissolved in aqueous HI solution (2 ml) and 50% aqueous H_3PO_2 (3.1 mmol) was added to the mixture. Separately, 2 mmol of phenethylamine were neutralized with 1 ml of HI 57% w/w causing the precipitation of a white solid that re-dissolved upon heating. This was added to the PbO solution, and the mixture heated at 150 °C under magnetic stirring on a hotplate. After 10 mins, the stirring was discontinued, and the solution was left to cool down at room temperature, causing the precipitation of orange crystals. These were collected by filtration and dried at 100 °C under vacuum. This synthesis process was adapted from the synthetic strategy reported by C. C. Stoumpos *et al.* [83] which used for similar layered perovskites.

B. Synthesis of $(PEA)_2(MA)$ $[Pb_2I_7]$ single crystal (n = 2)

2 mmol of PbO powder and 3 mmol of $MACl$ were dissolved in aqueous HI solution (2 ml) and 50% aqueous H_3PO_2 (3.1 mmol) was added to the mixture. Separately, 2 mmol of phenethylamine were neutralized with 1ml of HI 57% w/w causing the precipitation of a white solid that re-dissolved upon heating. This was added to the PbO solution, and the mixture heated at 150 °C under magnetic stirring on a hotplate. After 10 mins, the stirring was discontinued and the solution was left to cool down at room temperature, causing the precipitation of dark red crystals. These were collected by filtration and dried at 100 °C under vacuum. This synthesis process was adapted from the synthetic strategy reported by C. C. Stoumpos *et al.* [83] for similar layered perovskites.

C. Synthesis of $MAPbI_3$ single crystal (n = ∞)

Another similar procedure to that described by M. I. Saidaminov *et al.* was used for the synthesis of $MAPbI_3$. 1 M solution of PbI_2 and MAI was prepared in GBL. The solution was then left on the hotplate without stirring at 120 °C for 24 hours, allowing the growth of $MAPbI_3$ black crystals. These were recovered by filtration and dried at 100 °C in vacuum.

D. Synthesis of $(PEA)_2\,PbI_4$ (n = 1) thin film

0.5 M solutions of $(PEA)_2PbI_4$ were prepared by mixing stochiometric amounts of phenethylammonium iodide, $(PEA)I$ with PbI_2 in DMSO. After dissolving the powders at 100 °C for 1 hour, the solution was spin coated on p-doped silicon substrates at 4000 rpm for 30 seconds, and annealed at 100 °C for 15 minutes resulting in the formation of orange films.

E. Synthesis of multi-phase films $(PEA)_2(MA)_{n-1}$ $[Pb_nI_{3n+1}]$

The spin-coating solution was prepared in DMSO by mixing 1 M of $(PEA)I$, 0.5 M of MAI and 1 M of PbI_2. An initial molar ratio of 2:1:2 was used between $(PEA)I:MAI:PbI_2$. After dissolving the powders in solvent at 100 °C for 1 hour, the solution was spun coated on p-type silicon substrates at 4000 rpm for 30s then annealed at 100 °C for 15 minutes resulting in the formation of red films.

Chapter 3

Experimental Methods

3.1 Optical characterization measurements

3.1.1 UV-Vis Absorption measurement

The absorption spectra of the materials were measured using UV-Vis-NIR Spectrophotometer Shimadzu UV3600 (Figure 3-1). The samples were deposited on a glass substrate then were placed in the integrating sphere that was attached in the whole set up, with another glass substrates as reference. The materials were excited at 290 nm and measured by directing light in the wavelength range 300 nm to 900 nm and step increment of 1 nm onto the surface.

Figure 3-1. UV-Vis-NIR Spectrophotometer Shimadzu UV3600.

3.1.2 Photoluminescence and time-resolved photoluminescence measurement

A micro-photoluminescence setup was used to measure the photoluminescence spectra and time-resolved photoluminescence of the perovskite materials. This micro-PL setup is performed using free space excitation and collection using microscope objective (NA=0.3). Figure 3-2 illustrates the instrumental setup of photoluminescence measurement system. A ps-pulsed laser diode emitting at $405\ nm$ wavelength with 40 MHz repetition rate is used to excite the sample. The photoluminescence is collected by the objective lens and directed to a grating monochromator (Acton SpectraPro 2300i, Princeton Instruments) then spectrometer detector (Acton SpectraHub, Princeton Instruments) or time-correlated photon counting detector (PicoHarp 300, PicoQuant) with 4ps resolution.

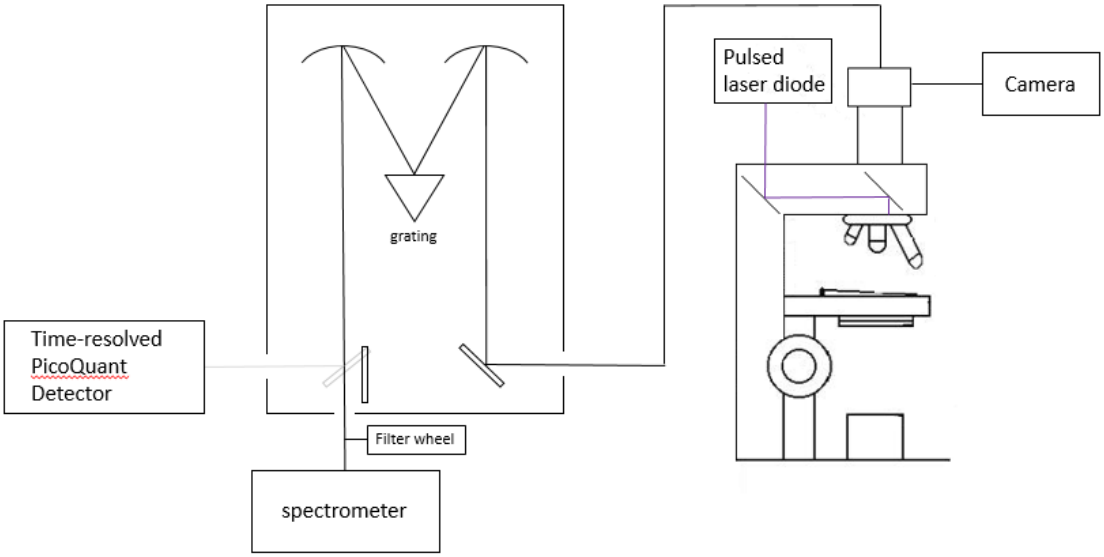

Figure 3-2. Instrumental setup of micro-photoluminescence system.

3.2 Cathodoluminescence measurements

3.2.1 Instrumental setup of Cathodoluminescence

The cathodoluminescence system used in this research was Allalin 4027 Chronos from Attolight AG. Figure 3-3 shows the instrumental setup of the microscope. The whole system is divided into four critical parts: field emission gun, hybrid electron and light objective, chamber and cryogenic stage and detectors.

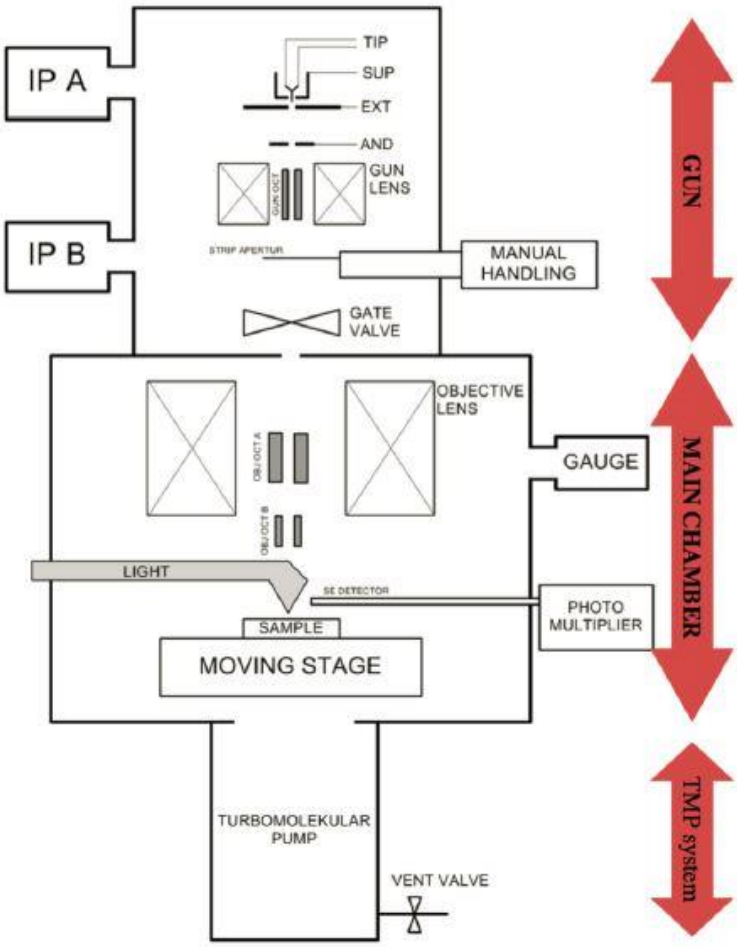

Figure 3-3. Instrumental setup of Allalin 4027 Chronos [84].

Firstly, a sharp tungsten filament is heated up. ZrO reservoir diffuses into the tungsten tip to lower the work function of the emitter such that the tip starts emitting electrons. The electrons are shaped by an extracted plate into cone shape then accelerated by an accelerator. Next, the electron beam passes through gun lens which control the size of the beam by controlling the probe current. This decides the number of electrons that reach the apertures. There are four apertures with different diameters (25, 30, 50 and 100 μm). Different apertures allow users to work in different probe current regimes. A manual handling is attached to the apertures to allow position tuning of the apertures. There are two ion pumps connected to the upper chamber to maintain ultrahigh vacuum ($1 \times 10^{-10}\ mbar$) to prevent contamination to the emission gun. The upper chamber (gun chamber) and the lower chamber (sample chamber) are separated by a separation valve to keep the gun chamber in ultrahigh vacuum during sample exchange.

The electron beam arrives at the objective lens when the separation valve is opened. The objective of this system is made up of a reflective objective and electromagnetic objective lens. A reflective objective with numerical aperture (NA) of 0.72 (half angle of 46°) is embedded within an electromagnetic objective, as illustrated in Figure 3-4. This reflective objective has high NA to collect cathodoluminescence effectively. The effective focal length of this objective is 7.2 mm. The electromagnetic lens is optimized to focus electrons at a working distance of 3 mm, which matches the focal plane of the light objective perfectly. This objective has large opening to allow the reflective objective to collect the luminescence from sample. Due to the large opening, the smallest achievable electron probe size is limited (2.7 nm at 10 kV).

The lower chamber can reach high vacuum ($< 1 \times 10^{-6}\ mbar$) through pumping by a turbomolecular pump. The turbomolecular pump contains a ventilation valve which is connected to the Nitrogen inlet. The chamber will be purged with Nitrogen during

sample exchange to reduce the amount of water and unwanted pollutants entering the chamber. The nano-positioning cryogenic stage (as illustrated in Figure A-1a in appendix) consists of specimen holder, nanopositioning stage and cryostat (for low temperature performance) with 6 degrees of freedom for arbitrary movements. A 25.4 mm diameter disc with three-points bayonet fitting (as illustrated in Figure A-1b) can be used to accommodate specimens. Note that the height of the specimen should be less than 1.5mm to prevent hitting the lens.

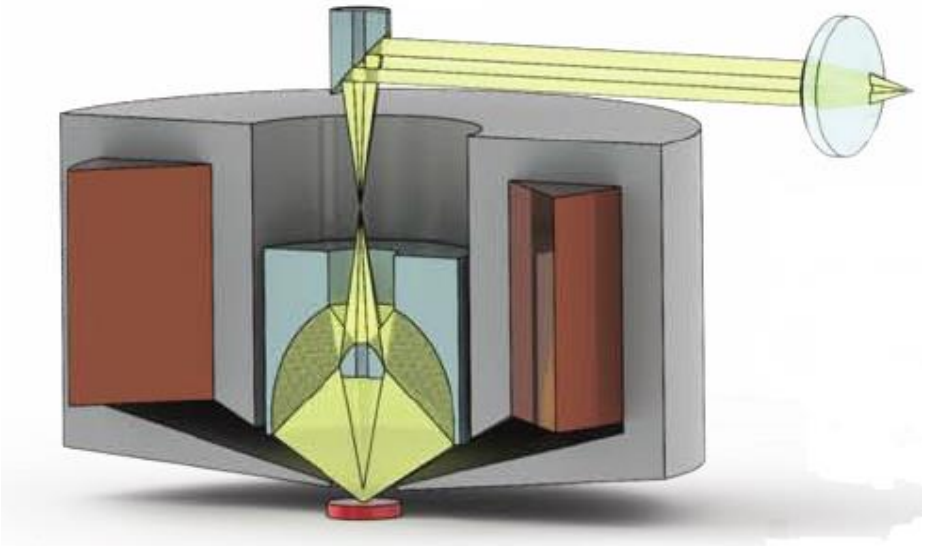

Figure 3-4. Hybrid electron and light objective of Allalin 4027 Chronos [85].

The detection system and time-resolved system are illustrated in Figure 3-5. The CL signals collected are directed to different detector depending on the acquisition range. Horiba Jobin Yvon iHR320 imaging spectrometer breaks down the CL signals in term of wavelength with three gratings on two different turrets. The information of the gratings is shown in Table A-1 in appendix. The detectors are placed at the exit slit. Spectroscopic CCD camera Newton920 can detect UV-VIS range from 180 – 1100 nm. Photodiode array InGaAs 490 detector covers near-IR range of wavelength from 600 – 1700 nm. A photomultiplier tube (PMT) is installed before the InGaAs detector.

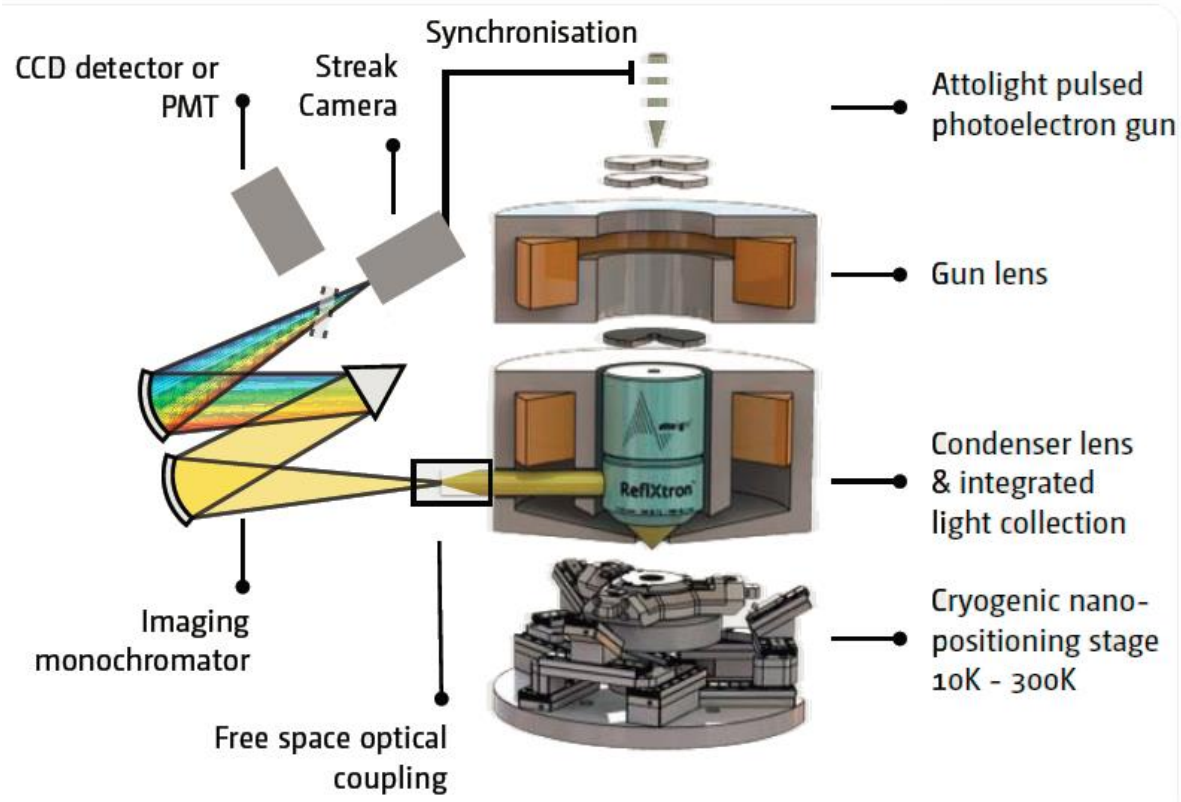

Figure 3-5. CL setup together with the time-resolved system and detection system [85].

A unique capability of this CL system is given by the operation in time-resolved mode. Traditional TRCL setup equipped a beam-blanking unit below the electron gun of SEM to generate electron pulses [66,67]. Due to the long duration of the electron pulse ($> 1\,ns$), the time resolution ($< 200\,ps$) of the traditional TRCL system is limited. To overcome this limitation, our CL system uses a photoemission-based electron gun. An ultrafast pulsed laser is employed to excite burst of electrons illuminating the cathode. Electron pulses are generated by a pulsed UV laser ($\lambda = 355nm$), with pulse duration < 2 ps . Optronis Optoscope SC-10 streak camera is used to collect photons emitted at range 200-850 nm, with temporal resolution >2ps. For IR detection, time correlated photon counting system is used. InGasAs/InP Single-Photon Avalanche Diode (SPAD) detector single detects photons with wavelength from 900-1700 nm, with timing jitter down to less than 100ps. Niobium Nitrite (NbN) superconducting nanowire single-

photon detector (SNSPD) is for detection of near-infrared single photons up to 2000 nm, with timing jitter less than 100ps.

3.2.2 Overcoming spatial resolution

The spatial resolution of cathodoluminescence maps is largely determined by three parameters: probe size (diameter of the focused electron beam), generation volume and diffusion length.

(a) Probe size

The smaller the probe size, the higher the resolution. The probe size is decided by the quality of gun lens, the spatial and energy profile of electrons emitted by electron gun, and working distance [86]. In this system, the probe size can be tuned from few nanometers up to micrometers.

(b) Generation volume

SE image resolution is weakly dependant on the generation volume. However, for visualization of CL signals (imaging or mapping), the spatial resolution is strongly determined by the interaction of the incident electrons and the material. The smaller the generation volume, the higher the spatial resolution. The generation volume depends on the properties of the material and the accelerating voltage. Accelerating voltage decides the energy of primary electrons and penetration depth of the electrons into the sample. However, low accelerating voltage also introduces the surface effect, where non-radiative processes dominate due to polishing damage, CL signal is hence effectively killed. It is also worth highlighting that small generation volume results in higher injection density (high charge carrier concentration in small volume) and lower CL emission due to saturation effect. Therefore, high spatial resolution requires optimum accelerating voltage and low beam current [86].

(c) Carrier Diffusion

The diffusion length of charge carriers directly affect the generation volume. The higher the carrier mobility or diffusion length, the lower the final resolution. The diffusion of the charge carriers is decided by the properties and quality of materials.

3.2.3 Overcoming time resolution

The time resolution of a CL system is often limited by the electron pulse duration and the temporal resolution of the detector. The detector used in the SPMS system, Optronis Optoscope SC-10 streak camera, carries intrinsic temporal resolution up to 2 ps (in ideal case). However, the actual resolution of the slit camera is affected by the parameters selected such as the aperture of temporal slit, the speed of jitter and the limited numbers of pixels of readout CCD in the streak camera. The electron pulse duration which acts as the opening of a "camera" shutter is also one of the limitations to the temporal resolution of the SPMS system. In order to obtain short electron pulse, the electron gun used in the CL system is photoemission-based electron gun. This photoemission-based electron gun is driven by a picosecond UV laser with pulse duration 5 - 7 ps. Electron pulses with similar duration should be generated, however, due to the Coulomb repulsion between the electrons (space charged effect) in the electron packet, electrons with different velocities arrive at the sample earlier or later, consequently develop temporal broadening during propagation. The time resolution of the CL system can be obtained by direct fitting and analysis of TRCL data of a stable material through introducing the Gaussian electron pulse profile into the fitting function [36] (refer to section 1.4.3). Based on the analysis done by the manufacturer, the electron pulses are broadened to around 10 ps upon arriving at samples. However, the actual time resolution of our CL system is around 20 ps. This is because there are many dispersive

spectroscopy instruments such as gratings in the system which affect the resolution of the signal obtained.

3.2.4 Cathodoluminescence and time-resolved cathodoluminescence measurement

Cathodoluminescence measurements were performed using Allalin 4027 Chronos from Attolight AG (Figure 3-6). The instrumental setup of Allalin 4027 Chronos has been shown in detail in previous section. Since the perovskites in this work have visible range bandgap, the measurements were performed by using grating with 150 gratings/mm and blazed at 500 nm. The spectra were acquired with Newton920 CCD with resolution 0.5 nm with different range depending on the emission of the materials. For every measurement, the electron beam was accelerated at 6 kV, passing through gun lens 1.2A. For time-resolved mode, 10 ps pulsed photoelectron gun was used. Perovskite films for CL were spin coated on p-doped silicon substrates.

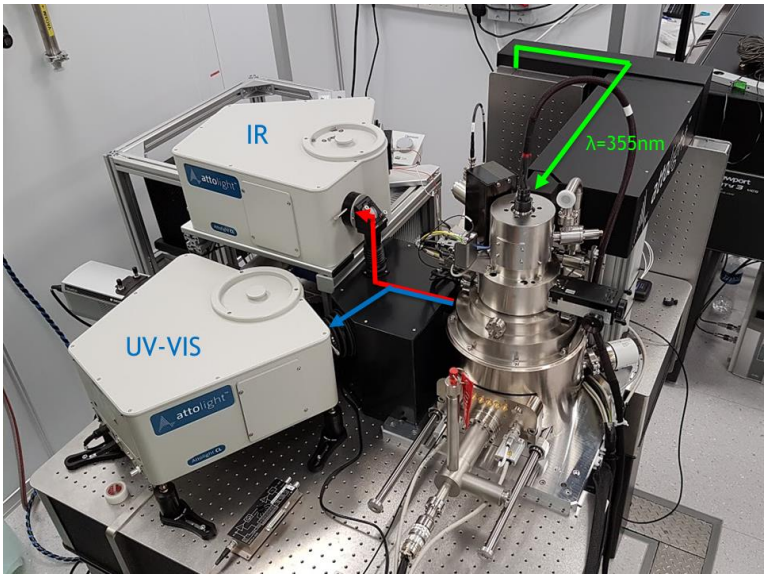

Figure 3-6. Attolight Allalin 4027 Chronos, Time Resolved Cathodoluminescence Microscope. Green arrow indicates the UV pulsed laser that excites pulse electrons. Blue and Red arrows indicate the path of collected light to UV-Vis detector and IR detector respectively.

Chapter 4

Results and Discussions

4.1 Lead halide perovskites

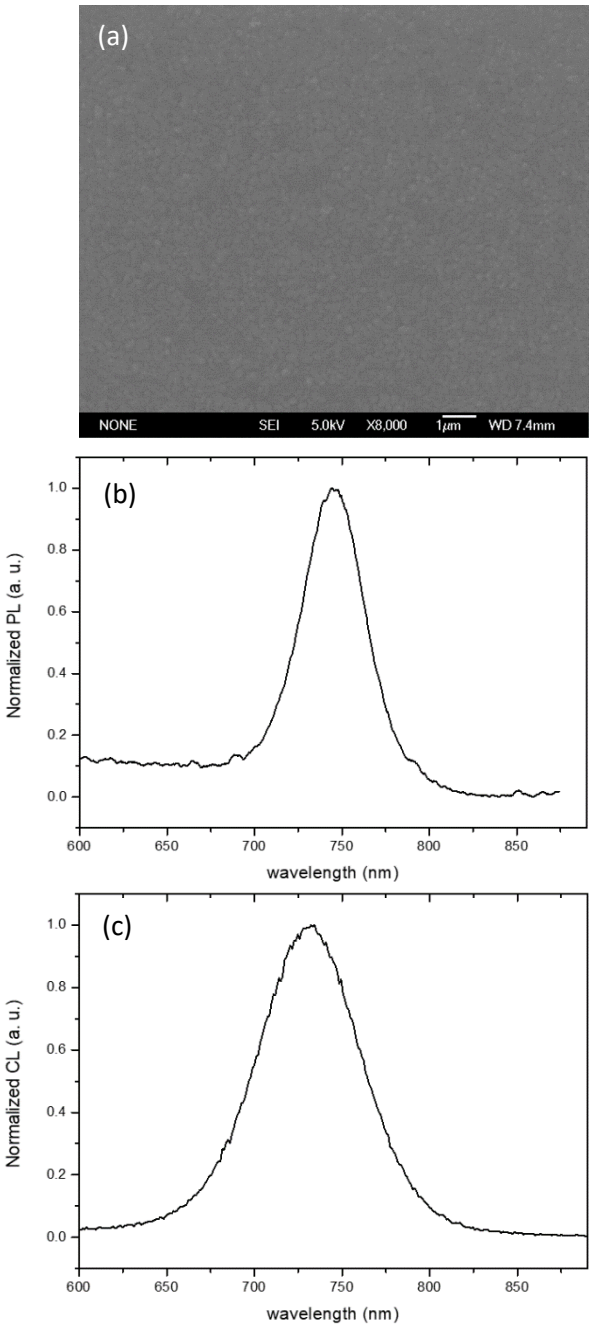

Figure 4-1. (a) SEM image and (b) PL spectrum and (c) CL spectrum of $MAPbI_3$.

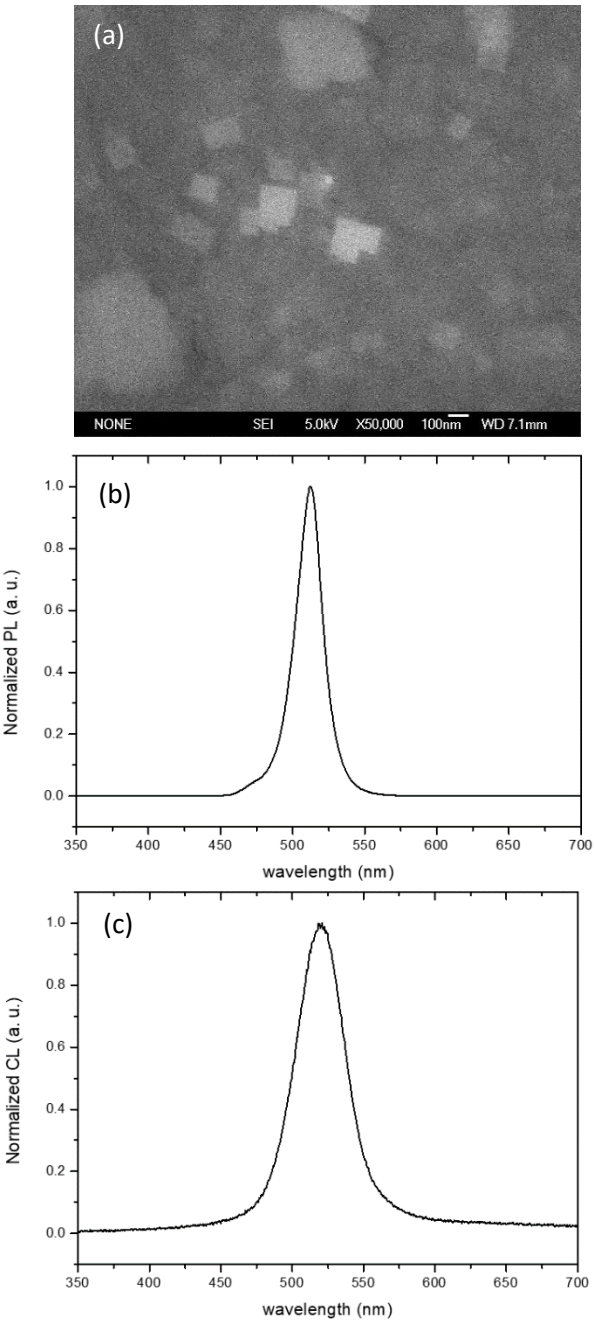

Figure 4-2. (a) SEM image and (b) PL spectrum and (c) CL spectrum of $CsPbBr_3$.

As mentioned in Section 2.2, the emission of $MAPbI_3$ and $CsPbBr_3$ were firstly studied to deal with the issue of stability of materials and resolution of signals, also as a calibration for our CL system. Figure 4-1a and 4-2a show the SEM images of $MAPbI_3$ thin film and $CsPbBr_3$ QDs respectively. PL emission spectrum of $MAPbI_3$ (Figure 4-1b) shows emission peak at 744 nm whereas CL emission spectrum of $MAPbI_3$ (Figure 4-1c) shows a strong emission peak at $738\ nm$. Nevertheless, the obtained CL peak is $1.68\ eV$ in energy scale. Comparing with the band gap value ($1.58\ eV$) obtained in previous work by SPMS research group [67], the energy of released photon is higher than the band gap. This might because the structure of $MAPbI_3$ is slightly oriented by high energy electron beam, the band gap of the material is broadened. PL emission spectrum of $CsPbBr_3$ (Figure 4-2b) shows emission peak at 512 nm whereas CL emission spectrum of $CsPbBr_3$ (Figure 4-2c) shows even stronger emission peak at $518\ nm$. It agrees reasonably with the results of reference literature [81] that we adapted for the synthesis method. Overall, the FWHM of the CL emission peaks are larger than that of PL emission peaks. Broadening of CL emission peaks is caused by the incident electrons which have excited more vibrational modes. Broadening will also be observed in the $(PEA)_2(MA)_{n-1}$ $[Pb_nI_{3n+1}]$ perovskites and will be further explained in next section.

4.2 Two-dimensional perovskite $(PEA)_2(MA)_{n-1}Pb_nI_{3n+1}$

Two-dimensional perovskite quasi-2D thin film was believed to contain several phases in single film hence allow energy funnelling effect, this claim has yet to be proven, hence it would be extremely interesting to reveal the spatial distribution of the film.

4.2.1 Single crystals

Perovskite single crystals were used to assign the individual phases distinguished the self-organized heterogeneous phases in the perovskite thin film and find their

characteristic emission spectra and decay dynamics as function of the thickness of inorganic layer. Without this information, it is not possible to identify the individual emissions states that were observed in the heterogeneous phases of perovskite. To obtain the absolute information of each states, single crystals of $(PEA)_2PbI_4$ (n = 1), $(PEA)_2(MA)[Pb_2I_7]$ (n = 2) and $MAPbI_3$ (n = ∞) were synthesized. Figure 4-3 shows the images of single crystals fabricated.

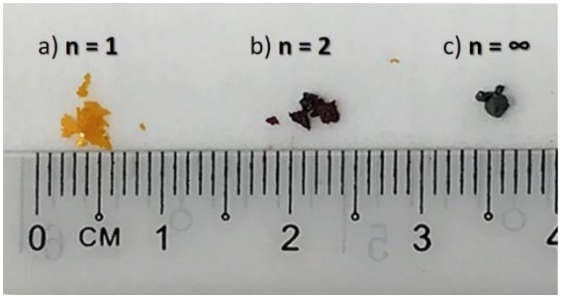

Figure 4-3. $(PEA)_2(MA)_{n-1}Pb_nI_{3n+1}$ perovskite single crystals: a) $(PEA)_2PbI_4$, n = 1, orange; b) $(PEA)_2(MA)[Pb_2I_7]$, n = 2, dark red; c) $MAPbI_3$, n = ∞, black.

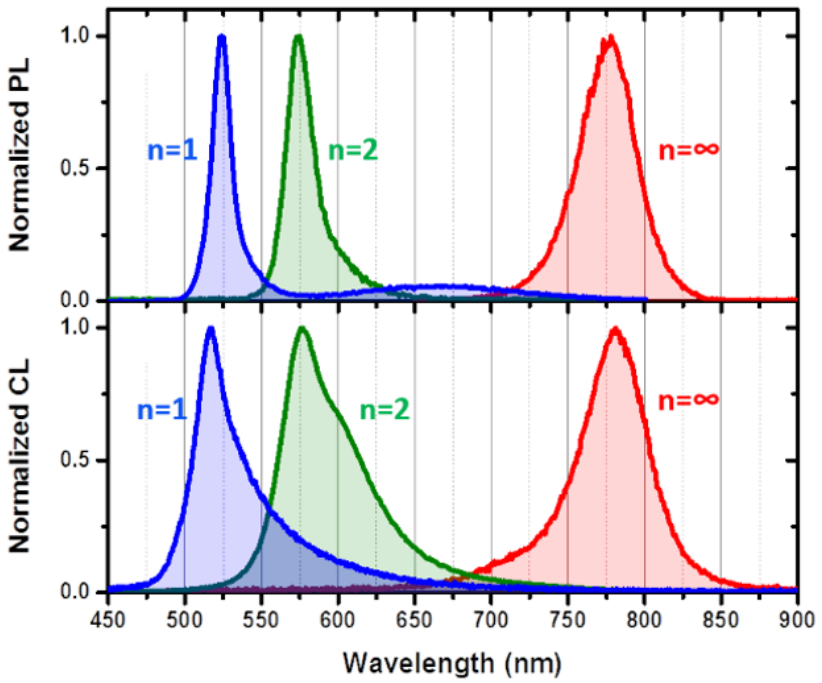

Figure 4-4. Photoluminescence and cathodoluminescence spectra of single crystals $(PEA)_2(MA)_{n-1}$ $[Pb_nI_{3n+1}]$ with n = 1, 2 and ∞.

PL and CL emission spectra of single crystals $n = 1$, $n = 2$ and $n = \infty$ are shown in Figure 4-4. It is observed that the CL emission peak for $(PEA)_2(MA)_{n-1}$ $[Pb_nI_{3n+1}]$ with $n = 1$ is slightly blue-shifted, whereas the CL emission peaks for $(PEA)_2(MA)_{n-1}$ $[Pb_nI_{3n+1}]$ with $n = 2$ and $n = \infty$ are red shifted when compared with their respective PL emission peaks. For the main reason for the inconsistency results (emission peaks fluctuate by few nm) in each CL acquisition, El-Hajjie et al. showed that both photo- and electroluminescence are spatially not uniform in perovskite [87]. The range of emitted photons fluctuate by ± 10 nm when investigated spatially at μm length scale. One of the possible explanations for red-shifting is the existence of shallow trapping levels where the recombination processes take part, hence emitting photons with lower energy.

Besides that, in cathodoluminescence, most of the energy of the incident electrons is converted to heat energy. The vibrational energy of atoms increases with temperature, causing the interatomic distances to become further and reducing the potential seen by the electrons in material, resulting in the narrowing of band gap. The observed blue-shifting of the CL emission peak for $(PEA)_2(MA)_{n-1}$ $[Pb_nI_{3n+1}]$ with $n = 1$ could be due to Burstein-Moss effect. Burstein-Moss effect occurs when the charge carrier concentration is much higher than the density of states in conduction or valence band, causing the Fermi level lies in conduction band or valence band. Consequently, the measured band gap appears to be larger than its actual value. The value of measured band gap is the sum of actual band gap and Burstein-Moss shift (see Figure 4-5).

Overall, the FWHM of the CL emission peaks are larger than that of PL emission peaks. Broadening and tailing of CL emission peaks is caused by is the incident electrons which have excited more vibrational modes. The relaxation to higher vibrational sublevels of electronic ground state (Figure 4-6), as the excitation energy from electron beam (few

keV) is relatively high compared to light excitation mode in photoluminescence. Another possible reason is more inter-band trapping states and vacancies are introduced by high energy electron, causing the emission peaks broader. Last but not least, it is also worth mentioning that the CL emission peak of $(PEA)_2(MA)_{n-1}$ $[Pb_nI_{3n+1}]$ with n = 2 has a shoulder peak at 600nm, as shown in Figure 3. We proposed that the crystallographic structure of small components of the perovskites were distorted by the high energy electron beam, from n = 2 phase to higher order phase. Nevertheless, the emission peaks for both PL and CL of these three materials almost coincide and lay well within the expectation values for the reported band gaps of these materials (PL emission peak of single crystals $n = 1$ is at $517\,nm$, $n = 2$ is at $570\,nm$ and $n = \infty$ at $781\,nm$) [88][89]. The emission peaks of $n = 1$, $n = 2$ and $n = \infty$ single crystals are $(520.0 \pm 5.0)nm$, $(575.5 \pm 0.5)nm$ and $(779.0 \pm 1.0)nm$ respectively. Their calculated bandgaps are hence 2.38 eV, 2.15 eV and 1.59 eV.

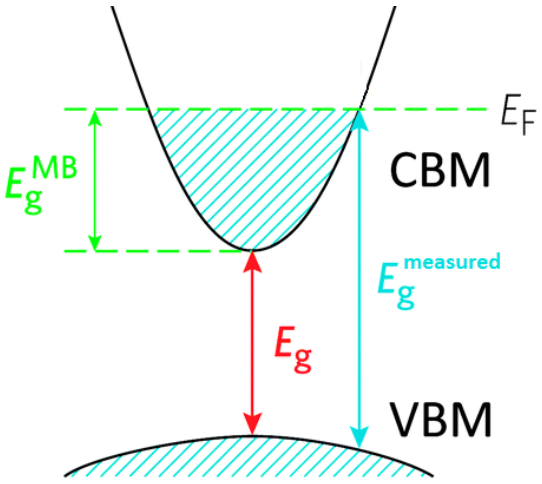

Figure 4-5. Optical band gap widening due to Burstein-Moss shift. Adapted from Ref. [91]

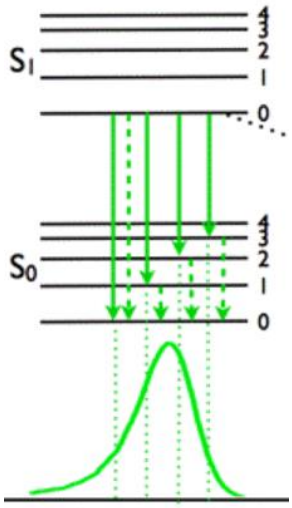

Figure 4-6. Jablonski diagram showing vibrational relaxation. [90]

4.2.2 Thin films

A. $(PEA)_2$ PbI_4 thin film (2D, pure n = 1)

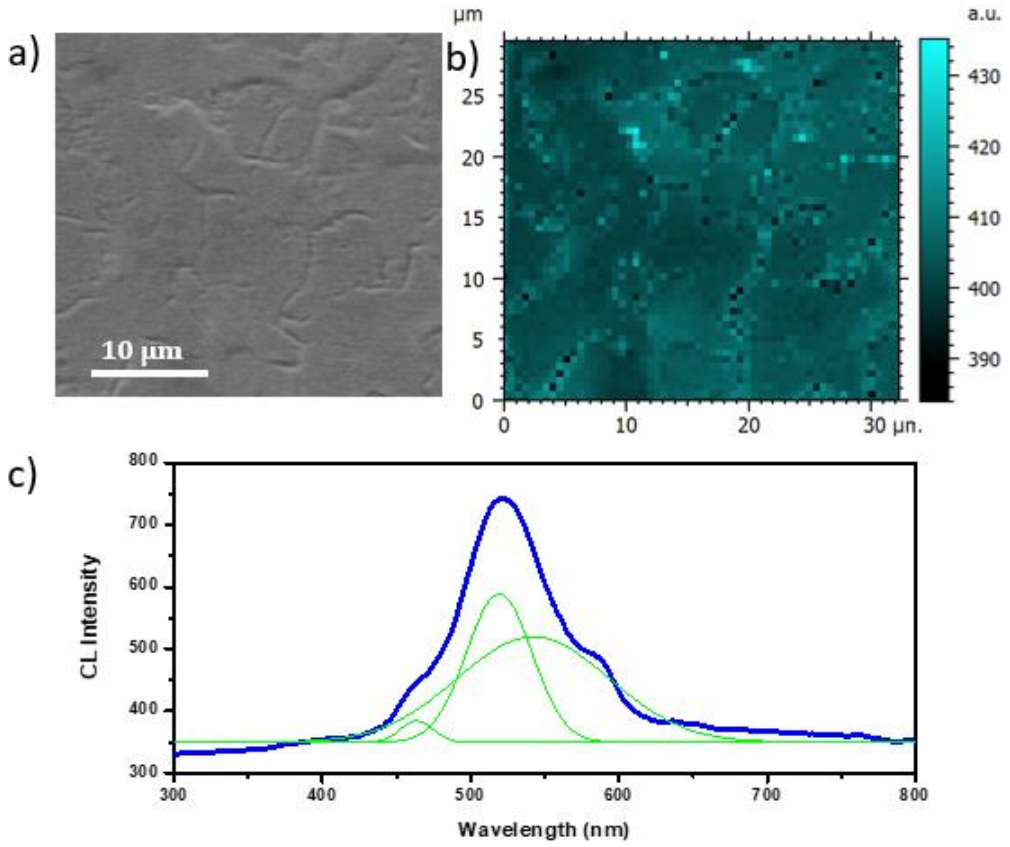

Figure 4-7. (a) SEM image, (b) CL map at 525 nm, (c) CL emission spectrum of $(PEA)_2PbI_4$ film.

Figure 4-7a shows the SEM image of n = 1 thin film, with corresponding CL emission intensity mapping in Figure 4-7b. CL emission spectrum is shown in Figure 4-7c. Pure $(PEA)_2PbI_4$ polycrystalline film exhibits cathodoluminences emission peaked around 520 nm. The intensity has been integrated between 515 nm to 525 nm. Directly comparing the CL map to the SEM image reveals a correlation between the cathodoluminescence intensity and the grains distributions --- lowly emissive areas (black colour in Figure 4-7b) correspond to the boundaries between the grains. There are several small parts with relatively higher emission (bright green colour in Figure 4-7b). This indicates inhomogeneity in the film crystallization. The main CL emission of

$(PEA)_2PbI_4$ thin film (Figure 4-8a) was at 520 nm. Comparing the PL emission spectrum and CL emission spectrum (Figure 4-8a and Figure 4-8b) of $(PEA)_2PbI_4$ thin film respectively, both CL and PL measurement come into agreement that they emit at the same wavelength. In Figure 4-8b, $(PEA)_2$ PbI_4 is observed that it mainly absorbs at 510 nm and emits at 520 nm. The different between band maxima in absorption and emission spectra can be explained by Kasha's rule. Some energy is lost by nonradiative relaxation process, consequently the emitted photons has less energy than absorbed photon, resulting in Stokes' shift.

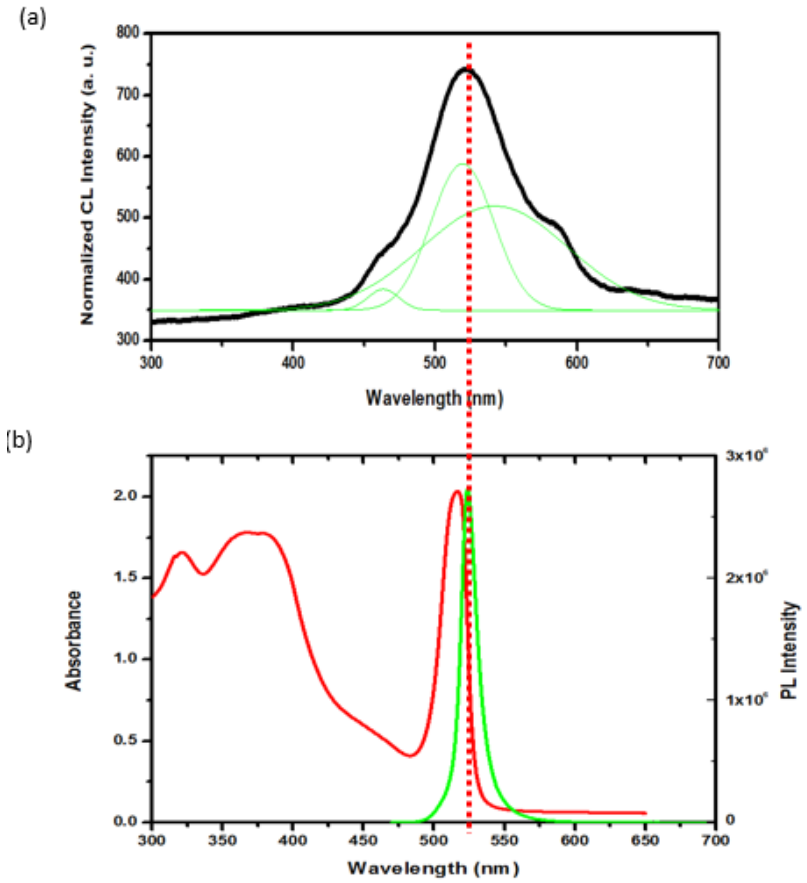

Figure 4-8. (a) CL spectrum and (b) Absorbance spectrum and PL spectrum of $(PEA)_2$ PbI_4 thin film.

B. Multi-phase $(PEA)_2(MA)_{n-1}$ $[Pb_nI_{3n+1}]$ film (quasi 2D, mixed n's)

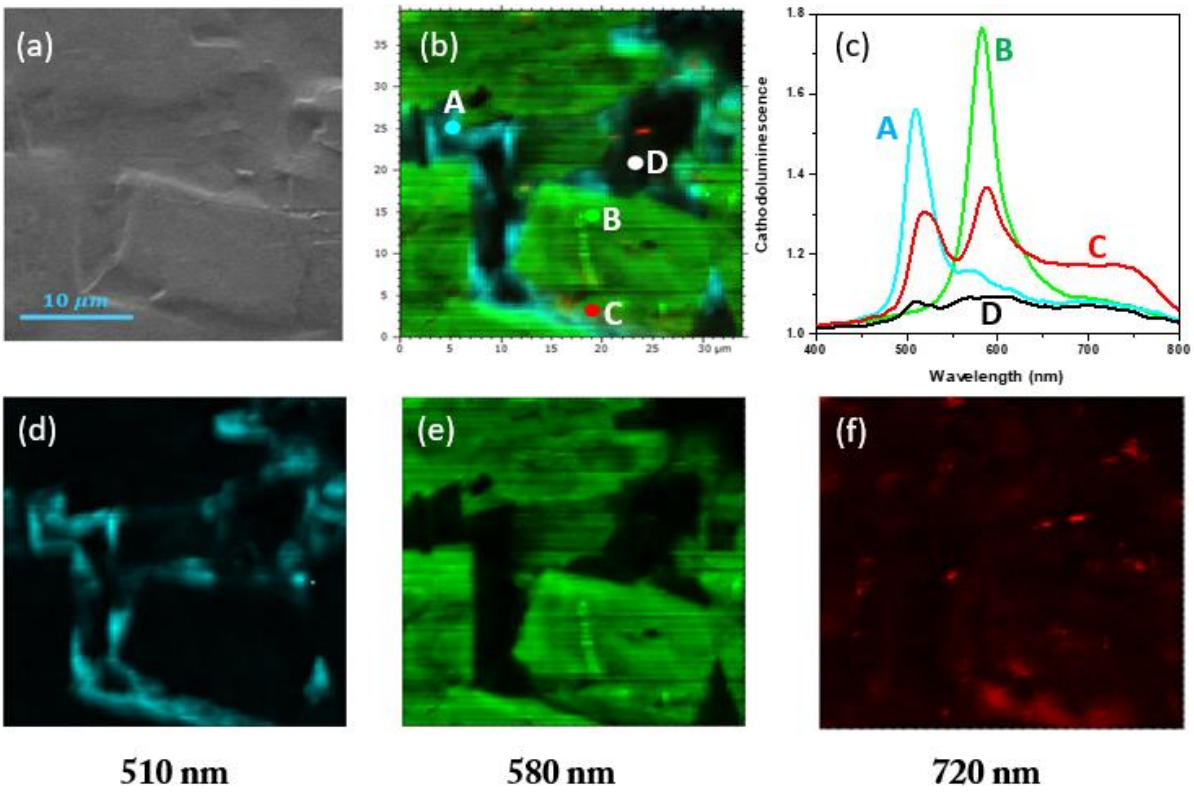

Figure 4-9. (a) SEM image of the multiphase $(PEA)_2(MA)_{n-1}[Pb_nI_{3n+1}]$ perovskite film and (b) corresponding cathodoluminescence (CL) map. (c), (d) and (e) maps show the individual CL components centered at 510 nm, 580 nm and 720 nm, respectively. (f) Spatially resolved CL spectra at specific points of the CL map (b).

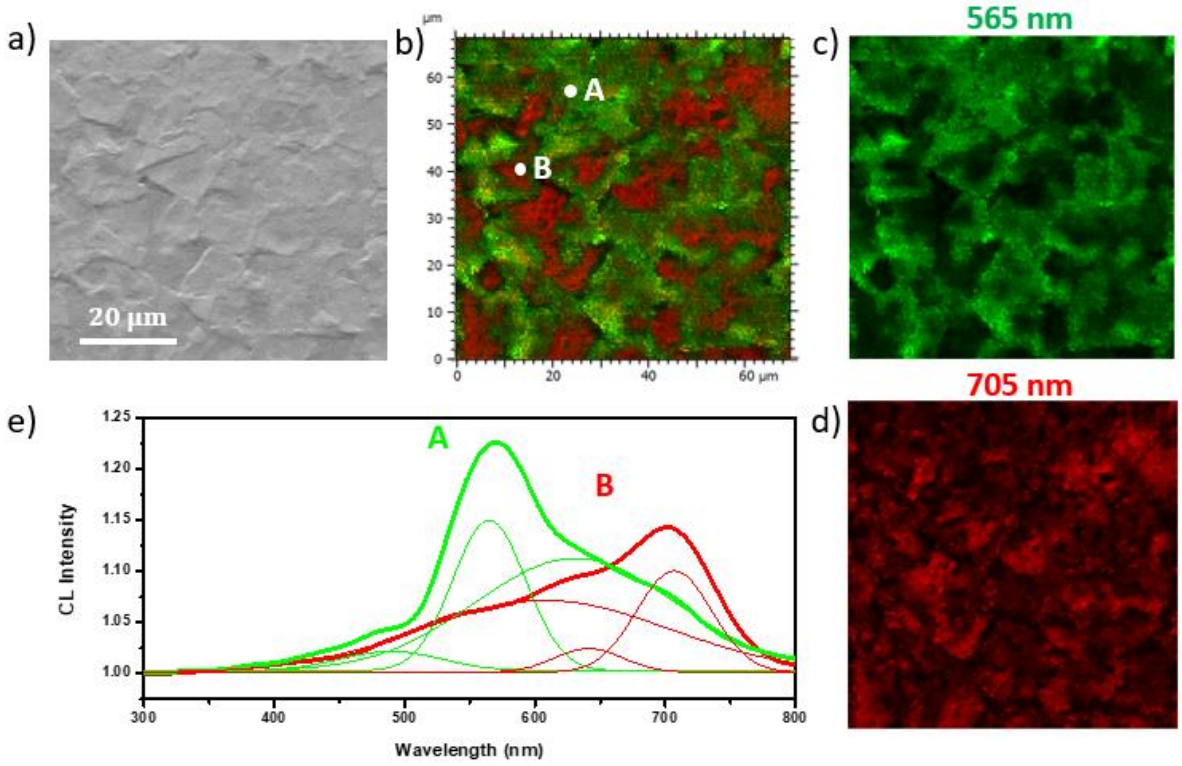

Figure 4-10. (a) SEM image of the multiphase $(PEA)_2(MA)_n[Pb_nI_{3n+1}]$ perovskite film and (b) corresponding cathodoluminescence (CL) map; (c) and (d) maps show the individual CL components cantered at 565 nm and 705 nm, respectively. (e) Spatially resolved CL spectra at point A and B of the CL map (b).

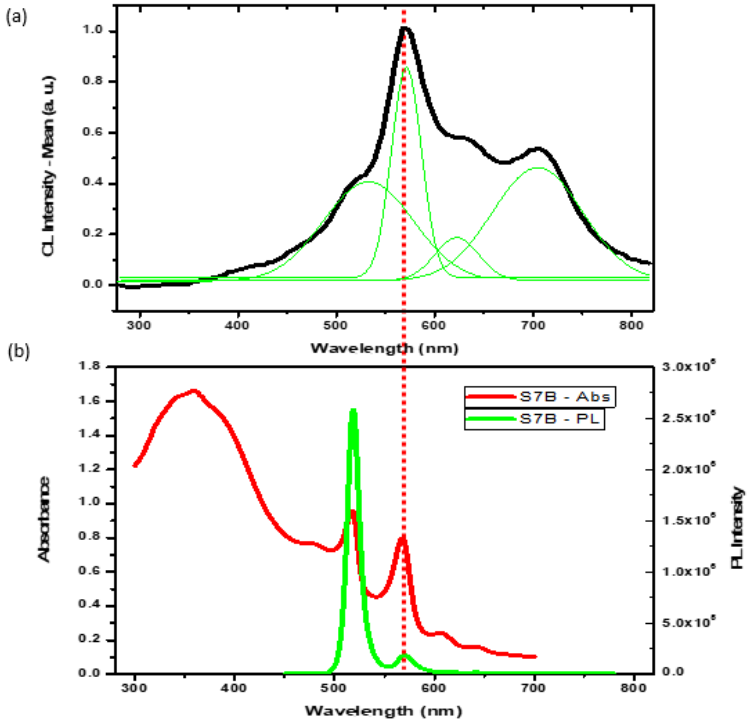

Figure 4-11. (a) CL spectrum and (b) Absorbance spectrum and PL spectrum of multi-phase thin film.

The absorption and emission spectra of two different regions in multi-phase perovskite thin film are summarized in Figure 4-9 and Figure 4-10. SEM image in Figure 4-9a shows the formation of an ensemble of flat, plate-like grains with edge length $> 10\ \mu m$ which appear uniform. CL mapping (Figure 4-9b) of the corresponding region reveals irregular luminescence across the probed area, yet following a well-defined pattern: at the crystal edges (point A), the emission is characteristic of the presence of $(PEA)_2PbI_4$ (n = 1), whereas the emission of the bulk of grains (point B) is typical of n = 2 phase $(PEA)_2(MA)[Pb_2I_7]$. Another weaker emission at $720nm$ is observed at the close proximity to the grain boundaries (point C) can be related to the formation of higher order phases ($n \geq 3$) of $(PEA)_2(MA)_{n-1}[Pb_nI_{3n+1}]$. Higher order single crystals ($n \geq 3$) were not fabricated by far in this work. According to the online references, single crystal $(PEA)_2(MA)_{n-1}[Pb_nI_{3n+1}]$ n = 3 has been fabricated and found to be emitted at 620 nm. This comes into agreement with Figure 4.10e and Figure 4-11a which shows the

emissions of multi-phase thin film are composed of peaks at 620 nm, indicates the trace amount of n = 3. The information of higher orders phases ($n \geq 4$) of $(PEA)_2(MA)_{n-1}[Pb_nI_{3n+1}]$ single crystals are currently not available. In another region of the same sample (Figure 4-10), phase segregation composed by perovskite clusters with lower and higher emission wavelength are found. The emission of certain grains at $705\ nm$ further indicates the formation of higher order phases of $(PEA)_2(MA)_{n-1}[Pb_nI_{3n+1}]$. In short, both Figure 4-9 and Figure 4-10 that show the SEM images and CL mapping at two different regions of the sample further confirm the existence of multiple grains. The grains show different emissions, meaning different grains are made of different number of layers of perovskites.

C. Time-resolved Cathodoluminescence

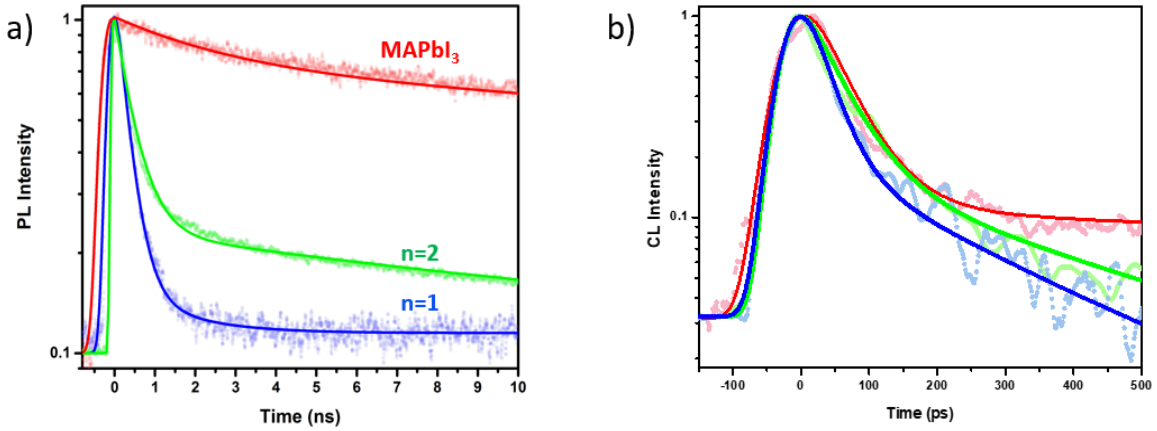

Figure 4-12. a) Time-resolved photoluminescence (λexc = 400 nm) and b) time-resolved cathodoluminescence measured on perovskite single crystals.

Table 4-1. Time resolved photoluminescence (TRPL) and cathodoluminescence (TRCL) fitting parameters for perovskite single crystals. TRPL decays are collected under 400 nm excitation wavelength; τ = characteristic lifetimes, A = amplitude.

Crystals	**Time-resolved PL**				
	λ (nm)	**A_1**	**τ_1 (ps)**	**A_2**	**τ_2 (ps)**
n = ∞	780	0.36	2657	0.64	44298
n = 2	575	0.83	450	0.17	14184
n = 1	525	0.97	298	0.03	1417
	Time-resolved CL				
n = ∞	780	0.96	50	0.04	2059
n = 2	575	0.89	49	0.11	380
n = 1	525	0.92	34	0.08	319

To study the lifetime and recombination dynamics of the perovskites, time-resolved CL measurement and time-resolved PL measurement was firstly performed on the single crystals (Figure 4-12). Table 4-1 gives the fits parameters of bi-exponential fits (Equation 4.1) of time-resolved data of single crystals in Figure 4-12.

$$y = y_0 + A_1 e^{-\frac{x-x_0}{\tau_1}} + A_2 e^{-\frac{x-x_0}{\tau_2}} \tag{4.1}$$

The fitting parameters obtained from the data of perovskite single crystals are used as reference for the assessment of the characteristic photoluminescence decay dynamics. The results in Figure 4-12 and Table 4-1 show that single crystals with increasing perovskite dimensionality exhibit progressively longer lifetime. The perovskite with dimensionality achieves infinity ($n = \infty$) exhibit a much longer lifetime component. Comparing the data of TRPL and TRCL of the single crystals, TRCL of the same perovskite crystals is dominated by a much faster decay. We suggest that this ultrafast decay is caused by the excitation by high energy electrons to hot-exciton thermalization and Auger recombination. Another interesting result is that the slower component (τ_2)

of TRCL well matches the faster component (τ_1) of TRPL of the same perovskite single crystals, suggesting they are related to the same recombination process.

Next, time-resolved cathodoluminescence (TRCL) measurements were performed on the pure phase $(PEA)_2PbI_4$ and multiphase $(PEA)_2(MA)_{n-1}[Pb_nI_{3n+1}]$ perovskite thin film. Table 4-2 shows the fits parameters of bi-exponential fits (Equation 4.1) of time-resolved data of pure phase and multiphase perovskite thin films in Figure 4-13. The film of pure $(PEA)_2PbI_4$ shows a single peak at 520 nm (Figure 4-13a), whereas the film of multiphase $(PEA)_2(MA)_{n-1}[Pb_nI_{3n+1}]$ shows multiple peaks at 520 nm (shorter lifetime) and 570 nm (longer lifetime), as obtained in Table 4-2. The higher dimensionalities component in the multiphase perovskite thin film could not be probed since the signals are too weak. The partial quenching of n = 1 component in multiphase perovskite thin film suggests that there exists energy transfer from lower dimensionalities (n = 1) to higher dimensionalities (n = 2). These results agree with the modelling introduced in Yuan's article as shown in Figure 2-5b and Figure 4-14 [80]. The energy funnelling effect is achievable in this film.

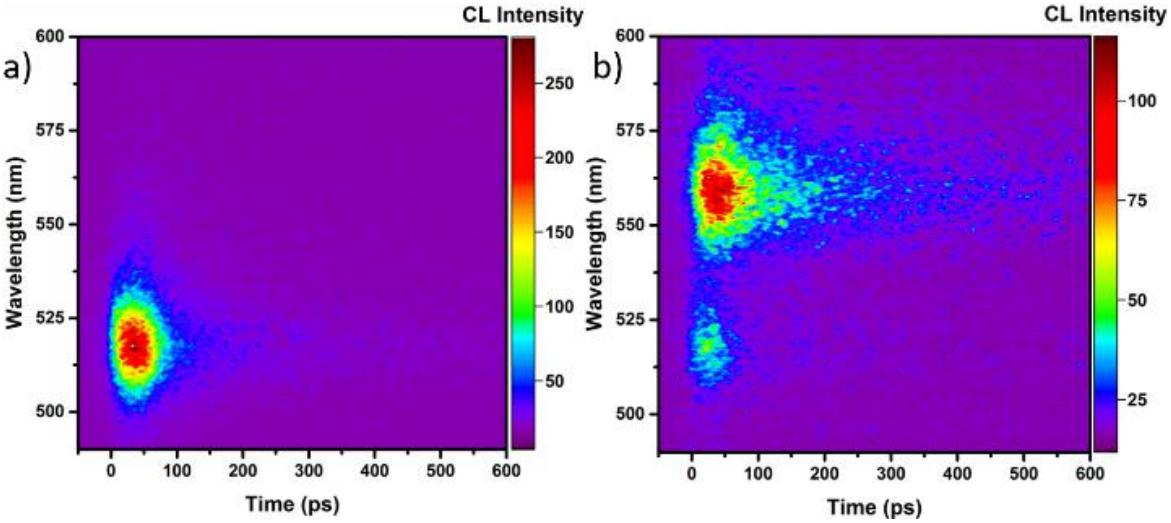

Figure 4-13. Time-resolved CL decays as a function of wavelength of (a) $(PEA)_2PbI_4$ (pure n = 1) thin film and (b) multi-phase $(PEA)_2(MA)_{n-1}$ $[Pb_nI_{3n+1}]$ thin film.

Table 4-2. Time resolved cathodoluminescence (TRCL) fitting parameters for perovskite films of pure $(PEA)_2PbI_4$ (n = 1) and multiphase$(PEA)_2(MA)_{n-1}$ $[Pb_nI_{3n+1}]$ film. In the last case, two main signals are probed relative to the n = 1 and n = 2 phases. τ = characteristic life-times, A = amplitude.

Thin Film	λ_{probe} (nm)	A_1	τ_1 (ps)	A_2	τ_2 (ps)
$(PEA)_2(MA)_{n-1}$ $[Pb_nI_{3n+1}]$	565	0.91	48	0.09	486
$(PEA)_2(MA)_{n-1}$ $[Pb_nI_{3n+1}]$	520	0.92	18	0.08	135
$(PEA)_2PbI_4$	520	0.96	31	0.04	308

Figure 4-14. Carrier transfer process in thin film perovskite with mixed states [80].

Chapter 5

Conclusions

Electron microscopes that operate in scanning mode combined with cathodoluminescence analysis are extraordinary tools for studying optical responses of nanostructures. In this work, the spatial distribution of the emission of perovskites allowed study of the relationship between the morphology and emission properties. Consequently, the 'band gap' can be mapped, revealing the relationship between the phases and luminescence. One can distinguish regions with n = 1, 2… *etc* from cathodoluminescence microscopy. The partial quenching of lower dimensionalities component in multiphase perovskite thin film also further proves the energy transfer from lower dimensionalities to higher dimensionalities. This self-assembled multicomponent and multi-layered quasi-2D perovskite enables convergence of excited carriers through funnelling mechanism hence increase the efficiency of radiative recombination and prolong the lifetime of emitted photons. This concept can be a potential breakthrough in improving the efficiencies of devices such as light emitting diode (LED) or solar cell by tailoring the composition of perovskites.

Chapter 6

Future Work

6.1 CL mapping of nanostructured perovskites

The rises in local photoluminescence emission after exposure to simulated sunlight has been presented in previous work. DeQuilettes *et al.* suggested that illumination induces redistribution of iodide and reduction of trap densities [92]. Their PL mapping (Figure 6-1) discovered that the changes in PL and trap densities are more significant for dimmer spots. CL mapping of nanostructured perovskite can reveal morphology emission characteristics and study the trap densities of materials under different conditions, such as different temperatures (different phases) and different exposure periods.

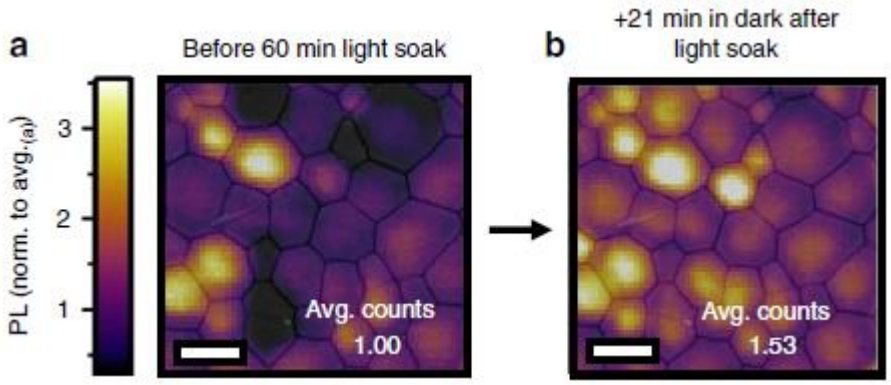

Figure 6-1. Local photoluminescence (PL) rises after exposure to simulated sunlight [92].

6.2 CL of perovskites metamaterials

A metamaterial is an arrangement of artificial structural elements designed to achieve advantages properties that are unachievable by natural materials. Thus far, metamaterial research has shown wide variety of extraordinary electromagnetic responses such as electromagnetically induce transparency (EIT), negative refractive index, and terahertz magnetism.[70,71,72] Plamons are the oscillations of electron gas plasma due to the coupling of incident electrons and electrons of metals. Localized surface plasmon (LSP) is formed when a surface plasmon is confined in a nanoparticle size comparable or smaller than the wavelength of excitation light. LSP can undergo radiative decay and release photons. Cathodoluminescence system can be used to study localized surface plasmon. With the advantage of spatial mapping ability of CL system, the surface plasmon resonance can be directly visualized. [25] The resonances at different wavelengths can also be determined. A recent work by B, Gholipourm, *et al.* demonstrates the first tunable-color perovskite $MAPbI_3$ across the visible range by nanostructuring them at subwavelength scales [96]. This overcomes the limitation of choice of materials and provides an alternative route other than varying perovskite composition chemically. Reflectivity of nanograting perovskite is effectively tuned by changing the grating period (Figure 6-2). Besides that, they also showed photoluminescence enhancement by nanopatterned perovskites. It will be extremely interesting to reveal the spatial distribution of the luminescence under CL system.

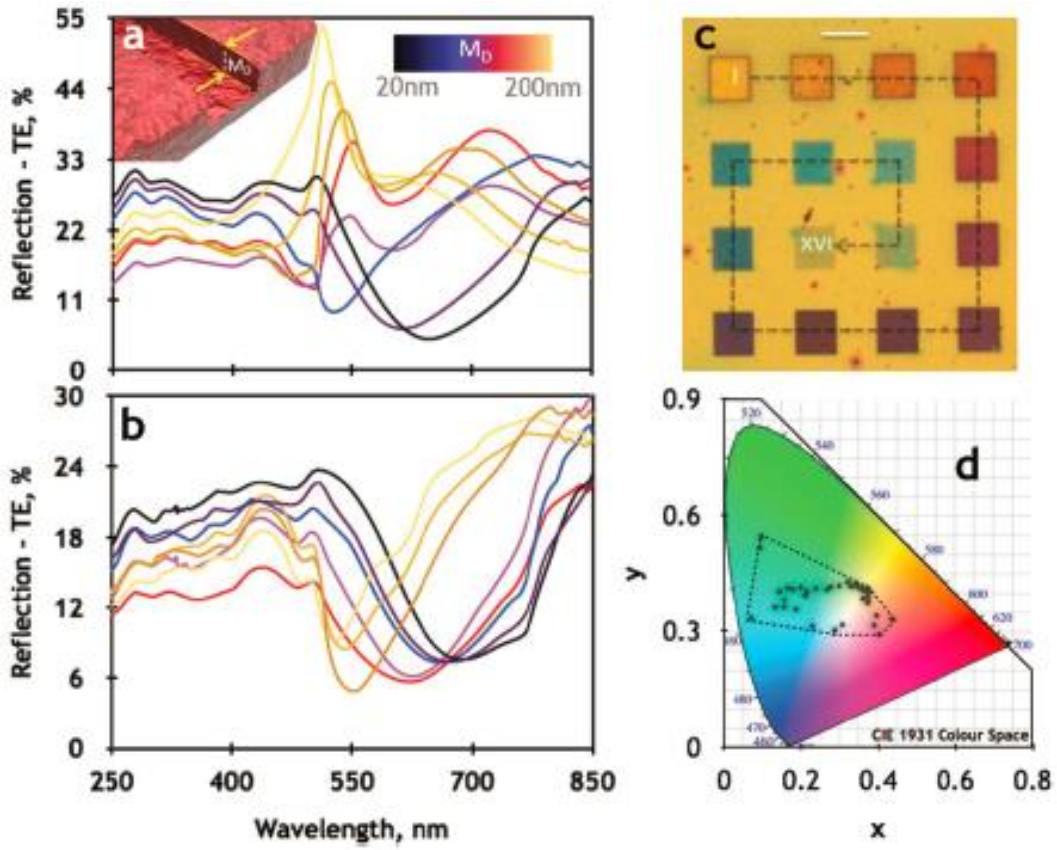

Figure 6-2. Tunable color perovskite metasurfaces. Reflection spectra of (a) nanograting and (b) nanoslit, with different etch depth. (c) Corresponding unpolarised optical microscope image of nanograting metasurfaces with different mill depth. (d) Color created by nanograting metasurfaces on CIE color palette. [96]

6.3 Electron-beam-induced current (EBIC)

Electron-beam-induced current (EBIC) is a semiconductor analysis technique performed in electron microscopy. It can be used to identify underlying junctions or defects in semiconductors and the characterization of minority carriers transport properties. Electron-hole pairs are generated upon excited by electron beam, then diffuse away from the generation volume due to the concentration gradient. An electric field is applied to separate the electron-hole pairs and the drifted charge carriers are collected. When an electric field is applied to an intrinsic semiconductor, the free electrons drift with velocity υ_e and the holes drift with velocity υ_h. They can be expressed in equation (6.1) and equation (6.2).

$$Drift\ velocity\ of\ electrons, \overrightarrow{v_e} = -\mu_e \vec{F} \tag{6.1}$$

$$Drift\ velocity\ of\ holes, \overrightarrow{v_h} = +\mu_h \vec{F} \tag{6.2}$$

where μ_e is the electron mobility, μ_h is the hole mobility and $\vec{F}$ is the electric field [97].

Even though the free electrons and the holes drift in opposite directions, their current densities add up together because their charge polarities are opposite.

Current density (current per unit area) can be expressed by equation (6.3).

$$Current\ density, J = env \tag{6.3}$$

where e is the electronic charge, n is the number of charge carriers per unit volume, υ is the drift velocity of the charge carriers. Since the drift velocity is directly proportional to the applied electric field, as shown in equation (6.1) and equation (6.2). By subbing equation (6.1) into equation (6.3), we get

$$Current\ density, J = en\mu F = \sigma F \tag{6.4}$$

where $\sigma = en\mu$ is the conductivity of the material.

EBIC can be mathematically modelled by considering the charge collection probability and the generation volume. Therefore, the normalized EBIC I_N can be expressed as:

$$\boldsymbol{I_N(x', z') = \iint Q(x, z) g(x - x', z - z') dx dz} \tag{6.5}$$

where $Q(x, z)$ is the charge collection probability and $g(x - x', z - z')$ is the generation volume centered at (x', z').

EBIC measurement is also accessible in the SPMS CL system, by contacting the specimens with the contact pads on the specimen holder. Another exciting opportunity is the time-resolved EBIC system which could achieve ultrafast current detection. EBIC of perovskite shows high electron extraction efficiency of perovskite-based solar cells. [98] However, the transport properties of charge carriers in perovskite are not in a complete story yet. EBIC mapping and time-resolved EBIC measurement are expected to reveal the transport properties and diffusion length of charge carriers in perovskites, relating with the morphology.

Appendix

Details of cathodoluminescence system

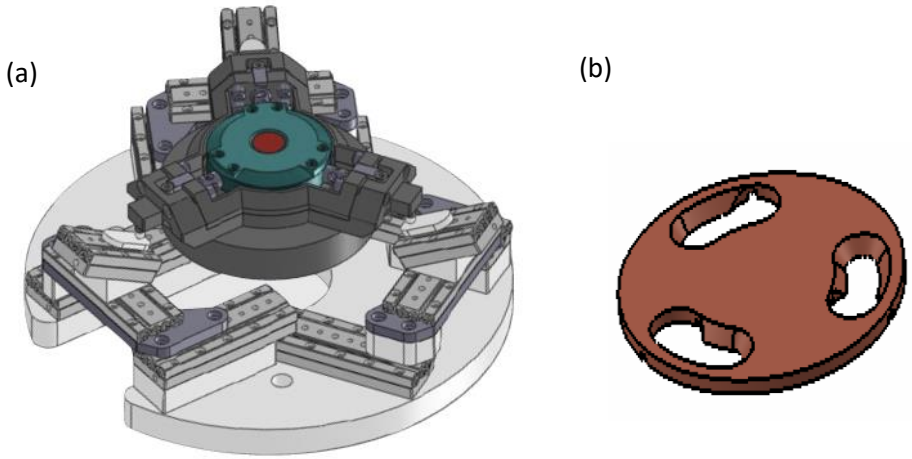

Figure A-1. (a) Cryogenic Nanopositioning stage and (b) specimen holder of Allalin 4027 Chronos. [99]

Table A-1. The information of turrets in spectrometer

Turret	Grating	Groove Density (gr/mm)	Blaze (nm)
1 (UV-Visible)	1.1	150	500
	1.2	600	300
	1.3	1200	250
2 (near-IR)	2.1	150	500
	2.2	600	750
	2.3	150	1200

A.1 Photomultiplier tube (PMT)

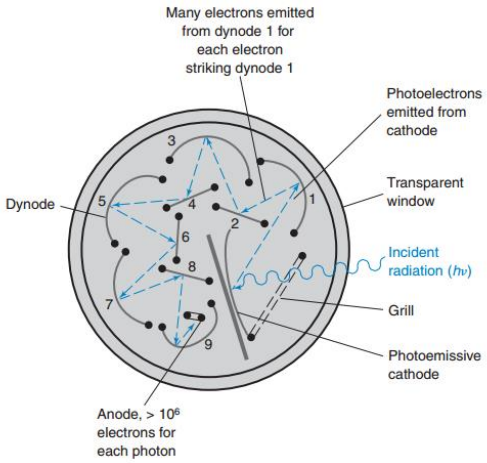

Figure A-2. Diagram of a photomultiplier tube with nine dynodes. [100]

A PMT (Figure A-2) is a sensitive device that amplifies the signals obtained. Firstly, the light falls on a photoemissive cathode, photoelectric effect causes the cathode emits electrons. The photoelectrons are accelerated towards secondary electrodes, called dynodes, and gain enough energy to knock off the secondary electrons. Each dynode amplifies signals by emitting more electrons. The process is repeated several times, the electrons are finally collected at the anode. In order to minimize the noise, it is necessary to operate PMT at low voltage. [101]

A.2 Photodiode Array (PDA)

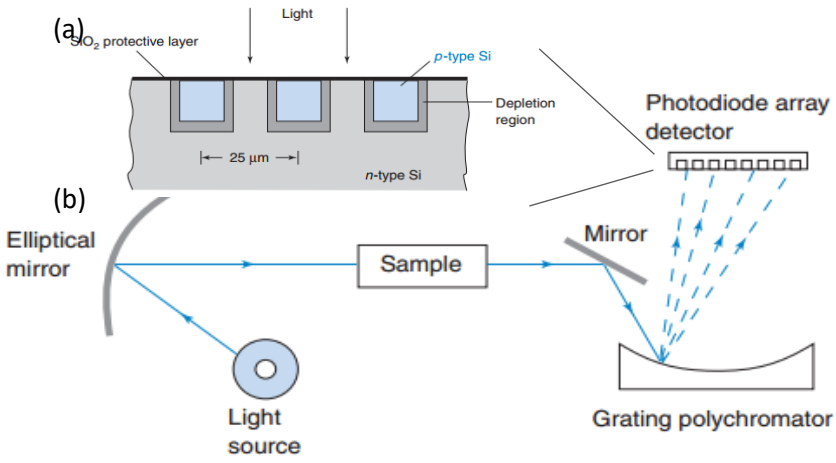

Figure A-3. (a) Schematic cross-sectional view of photodiode array. (b) Schematic design of PDA spectrophotometer. [100]

A photodiode array (PDA) consists of a linear of hundreds or thousands of photodiodes that convert the light into current. Figure A-3 shows the cross-sectional view of PDA. Rows of p-type silicon are embedded into n-type silicon substrate, creating a series of *pn* junction diodes. Electrons and holes are drawn away from the junction by applying reverse bias, hence the formation of depletion region, which act as condenser. These charges can be stored on the either side of depletion region. All diodes are fully charged at the start of measurement. During measurement, the incoming light excites electrons and partially discharge the condenser. The system obtains the information by detecting the current required to restore the charge. In practice, the light is dispersed into its component wavelength and directed to the diode array. Each diode detects the intensity of light at different wavelength simultaneously. Therefore, PDA allows high speed parallel readout. The resolution of PDA depends on the distance between the diodes and the dispersion of the grating polychromator.

A.3 Charge Coupled Device (CCD)

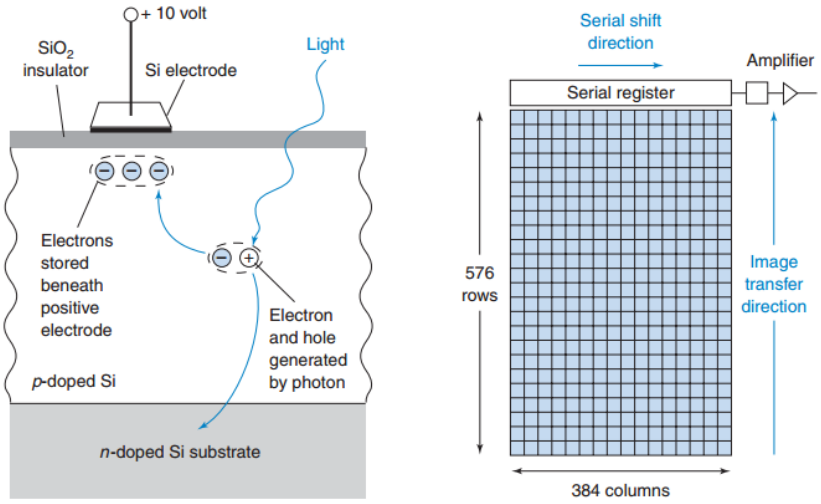

Figure A-4. (a) Cross sectional view of each pixel in CCD. (b) Top view of CCD. [100]

A charged coupled device (CCD) is extremely sensitive detector that consists of thousands of pixels in two-dimensional array (Figure A-4b). Each pixel is constructed of p-doped silicon on s-doped silicon substrate and conducting electrodes on top (Figure A-4a). Incoming light generate electrons and holes. The electrons are attracted and stored at the region beneath the positive electrode whereas the holes migrate to n-doped substrate. The electrical charge accumulated at each pixel is transferred to its neighbour pixel in horizontal direction, along the readout register, by applying bias. CCD has high quantum efficiency (electrons generated per incident photon), high sensitivity and low noise compared to readout signal.

Publication List

Articles:

1. *Cathodoluminescence of self-organized heterogeneous phases in Multidimensional Perovskites thin films,* D. Cortecchia,* **K.C. Lew,*** J.-K. So, A. Petrozza, C. Soci et al., in preparation (2017). *Chemistry of Materials* Article ASAP (2017). DOI: 10.1021/acs.chemmater.7b03851. *Equally contributing authors.

*Equally contributing authors.

2. *Nanopatterning-enhanced perovskite luminophore*, G. Adamo, B. Gholipour, **K.C. Lew**, D. Cortecchia, H.N.S. Krishnamoorthy, A. Bruno, J.-K. So, M.D. Birowosuto, N.I. Zheludev, C. Soci, CLEO Europe 2017, Munich (Germany), 25-29 June 2017 (accepted for oral presentation with proceedings).

Conference presentations:

1. *Color tunable perovskite metamaterials*, G. Adamo, B. Gholipour, **K.C. Lew**, D. Cortecchia, H.N.S. Krishnamoorthy, J.K. So, M.D. Birowosuto, N.I. Zheludev, C. Soci, The 8th International Conference on Surface Plasmon Photonics (SPP8), Taipei, Taiwan, 22-26 May 2017 (accepted for oral presentation)

2. *Cathodoluminescence spectroscopy of multidimensional organic-inorganic perovskites*, **K.C. Lew**, D. Cortecchia, J. So, A. Bruno, C. Soci, IPS Meeting 2017, Singapore, 22-24 February 2017 (talk).

3. *Control of luminescence in perovskite metamaterials*, G. Adamo, B. Gholipour, **K.C. Lew**, D. Cortecchia, H.N.S. Krishnamoorthy, A. Bruno, J.-K. So, M.D. Birowosuto, N.I. Zheludev, C. Soci, IPS Meeting 2017, Singapore, 22-24 February 2017 (invited talk).

4. Methylammonium lead iodide perovskite field-effect transistors, F. Maddalena, X.Y. Chin, **K.C. Lew**, D. Cortecchia, U.S. Binte Eliase, A. Bruno, C. Soci, IPS Meeting 2016, 7-8 March 2016, Singapore (poster).

5. Hybrid organic-inorganic perovskite nanostructures, **K.C. Lew**, D. Cortecchia, X.Y. Chin, P. Lova, A. Bruno, C. Soci, IPS Meeting 2016, 7-8 March 2016, Singapore (poster).

6. Plasmonic enhancement of spontaneous emission in metal-perovskite slabs, M.D. Birowosuto, D. Cortecchia, **K.C. Lew**, P. Lova, A. Bruno, C. Soci, IPS Meeting 2016, 7-8 March 2016, Singapore (poster).

References

[1] National Center for Photovoltaics (NCPV), "Cell efficiencies," *National Renewable Energy Laboratory (NREL)*, 2017. [Online]. Available: http://www.nrel.gov/ncpv/images/efficiency_chart.jpg.

[2] Z.-K. Tan, R. S. Moghaddam, M. L. Lai, P. Docampo, R. Higler, F. Deschler, M. Price, A. Sadhanala, L. M. Pazos, D. Credgington, F. Hanusch, T. Bein, H. J. Snaith, and R. H. Friend, "Bright light-emitting diodes based on organometal halide perovskite," *Nat Nano*, vol. 9, no. 9, pp. 687–692, Sep. 2014.

[3] G. Xing, N. Mathews, S. S. Lim, N. Yantara, X. Liu, D. Sabba, M. Grätzel, S. Mhaisalkar, and T. C. Sum, "Low-temperature solution-processed wavelength-tunable perovskites for lasing," *Nat. Mater.*, vol. 13, no. 5, pp. 476–480, 2014.

[4] C. Wehrenfennig, G. E. Eperon, M. B. Johnston, H. J. Snaith, and L. M. Herz, "High Charge Carrier Mobilities and Lifetimes in Organolead Trihalide Perovskites," *Adv. Mater.*, vol. 26, no. 10, pp. 1584–1589, Mar. 2014.

[5] G. Xing, N. Mathews, S. Sun, S. S. Lim, Y. M. Lam, M. Grätzel, S. Mhaisalkar, and T. C. Sum, "Long-Range Balanced Electron- and Hole-Transport Lengths in Organic-Inorganic CH3NH3PbI3," *Science (80-.).*, vol. 342, no. 6156, 2013.

[6] J. J. Thomson, "XL. *Cathode Rays*," *Philos. Mag. Ser. 5*, vol. 44, no. 269, pp. 293–316, Oct. 1897.

[7] M. Bellis, "Television History - Cathode Ray Tube," *About.com*. [Online]. Available: http://inventors.about.com/od/cstartinventions/a/CathodeRayTube.htm. [Accessed: 17-Jan-2017].

[8] B. G. Yacobi and D. B. Holt, *Cathodoluminescence Microscopy of Inorganic Solids*. Springer Science+Business Media New York, 1990.

[9] F. J. García De Abajo, "Optical excitations in electron microscopy," *Rev. Mod. Phys.*, vol. 82, no. 1, pp. 209–275, 2010.

[10] V. Myroshnychenko, J. Nelayah, G. Adamo, N. Geuquet, J. Rodríguez-Fernández, I. Pastoriza-Santos, K. F. MacDonald, L. Henrard, L. M. Liz-Marzán, N. I. Zheludev, M. Kociak, and F. J. García de Abajo, "Plasmon Spectroscopy and Imaging of Individual Gold Nanodecahedra: A Combined Optical Microscopy, Cathodoluminescence, and Electron Energy-Loss Spectroscopy Study," *Nano Lett.*, vol. 12, no. 8, pp. 4172–4180, Aug. 2012.

[11] M. V. Bashevoy, F. Jonsson, K. F. MacDonald, Y. Chen, and N. I. Zheludev, "Hyperspectral imaging of plasmonic nanostructures with nanoscale resolution," *Opt. Express*, vol. 15, no. 18, p. 11313, Sep. 2007.

[12] * Ernst Jan R. Vesseur, René de Waele, and Martin Kuttge, and A. Polman, "Direct Observation of Plasmonic Modes in Au Nanowires Using High-Resolution Cathodoluminescence Spectroscopy," 2007.

[13] N. Yamamoto, M. Nakano, and T. Suzuki, "Light emission by surface plasmons on nanostructures of metal surfaces induced by high-energy electron beams," *Surf. Interface Anal.*, vol. 38, no. 12–13, pp. 1725–1730, Dec. 2006.

[14] J. M. Kadro, K. Nonomura, D. Gachet, M. Grätzel, and A. Hagfeldt, "Facile route to freestanding CH3NH3PbI3 crystals using inverse solubility," *Sci. Rep.*, vol. 5, p. 11654, Jun. 2015.

[15] C. Xiao, Z. Li, H. Guthrey, J. Moseley, Y. Yang, S. Wozny, H. Moutinho, B. To, J. J. Berry, B. Gorman, Y. Yan, K. Zhu, and M. Al-Jassim, "Mechanisms of Electron-Beam-Induced Damage in Perovskite Thin Films Revealed by Cathodoluminescence Spectroscopy," *J. Phys. Chem. Lett.*, vol. 119, pp. 26904–26911, 2015.

[16] E. Horváth, M. Spina, Z. Szekrényes, K. Kamarás, R. Gaal, D. Gachet, and L. Forró, "Nanowires of Methylammonium Lead Iodide (CH3NH3PbI3) Prepared by Low Temperature Solution-Mediated Crystallization," 2014.

[17] M. I. Dar, G. Jacopin, M. Hezam, N. Arora, S. M. Zakeeruddin, B. Deveaud, M. K. Nazeeruddin, and M. Grätzel, "Asymmetric Cathodoluminescence Emission in $CH_3NH_3PbI_{3-x}Br_x$ Perovskite Single Crystals," *ACS Photonics*, p. acsphotonics.6b00290, 2016.

[18] L. Ozawa, *Cathodoluminescence : theory and applications*. Tokyo, Japan : Kodansha ;, 1990.

[19] S. Basu, *Crystalline Silicon - Properties and Uses*. InTech, 2011.

[20] E. Napchan, "Monte Carlo Simulation of Electron Trajectories," *Eur. Microsc. Anal.*, 1992.

[21] P. J. Potts, "Electron probe microanalysis," in *A Handbook of Silicate Rock Analysis*, Dordrecht: Springer Netherlands, 1987, pp. 326–382.

[22] M. Kasha, H. R. Rawls, and M. Ashraf El-Bayoumi, "The exciton model in molecular spectroscopy," *Pure Appl. Chem.*, vol. 11, no. 3–4, Jan. 1965.

[23] F. De Abajo and A. Howie, "Retarded field calculation of electron energy loss in inhomogeneous dielectrics," *Phys. Rev. B*, 2002.

[24] F. J. García de Abajo, "Relativistic energy loss and induced photon emission in the interaction of a dielectric sphere with an external electron beam," *Phys. Rev. B*, vol. 59, no. 4, pp. 3095–3107, Jan. 1999.

[25] G. Adamo, "Free-electron-driven nanoscale light sources: from Hertzian antennas to metamaterials," University of Southampton, 2011.

[26] A. I. Denisyuk, "Cathodoluminescence and Phase-change Functionality of Metallic Nanoparticles," University of Southampton, 2009.

[27] B. J. M. Brenny, T. Coenen, and A. Polman, "Quantifying coherent and incoherent cathodoluminescence in semiconductors and metals," *J. Appl. Phys.*, vol. 115, no. 24, p. 244307, Jun. 2014.

[28] U. Vetter, H. Hofsäss, and T. Taniguchi, "Visible cathodoluminescence from Eu-implanted single-and polycrystal c-BN annealed under high-temperature, high-pressure conditions," *Appl. Phys. Lett.*, 2004.

[29] S. Khatsevich, D. Rich, X. Zhang, and W. Zhou, "Temperature dependence of excitonic recombination in lateral epitaxially overgrown InGaN/GaN quantum wells studied with cathodoluminescence," *J. Appl.*, 2004.

[30] J. Kelly, H. P. Kuo, B. M. Oliver, J. D. Foster, and W. C. Haase, "Electron beam blanker." Google Patents, 24-Apr-1984.

[31] R. J. Moerland, I. Gerward, C. Weppelman, M. W. H. Garming, P. Kruit, and J. P. Hoogenboom, "Time-resolved cathodoluminescence microscopy with sub-nanosecond beam blanking for direct evaluation of the local density of states."

[32] S. Collin, M. Merano, M. Gatri, S. Sonderegger, P. Renucci, J.-D. Ganière, and B.

Deveaud, “Transverse and longitudinal space-charge-induced broadenings of ultrafast electron packets,” *J. Appl. Phys.*, vol. 98, no. 9, p. 94910, Nov. 2005.

[33] S. Sonderegger, “Picosecond Time Resolved Cathodoluminescence to Study Semiconductor Materials and Heterostructures,” ÉCOLE POLYTECHNIQUE FÉDÉRALE DE LAUSANNE, 2007.

[34] “Dynamic Process in Biology, Chemistry, and Materials Science: Opportunities for UltraFast Transmission Electron Microscopy,” 2011.

[35] Hamamatsu, “Guide to Streak Cameras,” 2008.

[36] M. Merano, “Picosecond Cathodoluminescence,” ÉCOLE POLYTECHNIQUE FÉDÉRALE DE LAUSANNE, 2005.

[37] J. C. Williamson, M. Dantus, S. B. Kim, and A. H. Zewail, “Ultrafast diffraction and molecular structure,” *Chem. Phys. Lett.*, vol. 196, no. 6, pp. 529–534, Aug. 1992.

[38] J. C. Williamson, J. Cao, H. Ihee, H. Frey, and A. H. Zewail, “Clocking transient chemical changes by ultrafast electron diffraction,” *Nature*, vol. 386, no. 6621, p. 159, 1997.

[39] V. A. Lobastov, R. Srinivasan, and A. H. Zewail, “Four-dimensional ultrafast electron microscopy,” *Proc. Natl. Acad. Sci. U. S. A.*, vol. 102, no. 20, pp. 7069–7073, 2005.

[40] D. J. Flannigan, B. Barwick, and A. H. Zewail, “Biological imaging with 4D ultrafast electron microscopy,” *Proc. Natl. Acad. Sci.* , vol. 107, no. 22, pp. 9933–9937, Jun. 2010.

[41] A. H. Zewail, “Four-Dimensional Electron Microscopy,” *Science (80-.).*, vol. 328, no. 5975, 2010.

[42] M. Aidelsburger, F. O. Kirchner, F. Krausz, and P. Baum, “Single-electron pulses for ultrafast diffraction.,” *Proc. Natl. Acad. Sci. U. S. A.*, vol. 107, no. 46, pp. 19714–9, Nov. 2010.

[43] P. Hommelhoff, C. Kealhofer, and M. A. Kasevich, “Ultrafast electron pulses from a tungsten tip triggered by low-power femtosecond laser pulses,” *Phys. Rev. Lett.*, vol. 97, no. 24, p. 247402, 2006.

[44] M. W. Davidson, “Photomicrography in the Geological Sciences.,” *J. Geol. Educ.*, vol. 39, no. 5, pp. 403–418, 1991.

[45] V. M. Goldschmidt, “Die Gesetza der Krystallochemie,” *Naturwissenschaften*, vol. 14, no. 21, pp. 477–485, 1926.

[46] H. D. Megaw, “Crystal structure of double oxides of the perovskite type,” *Proc. Phys. Soc.*, vol. 58, no. 2, pp. 133–152, Mar. 1946.

[47] H. J. Snaith, “Perovskites: The Emergence of a New Era for Low-Cost, High-Efficiency Solar Cells,” *J. Phys. Chem. Lett.*, vol. 4, no. 21, pp. 3623–3630, Nov. 2013.

[48] J. G. Bednorz and K. A. Müller, “Possible high Tc superconductivity in the Ba-La-Cu-O system,” *Zeitschrift für Phys. B Condens. Matter*, vol. 64, no. 2, pp. 189–193, Jun. 1986.

[49] D. B. Mitzi, K. Chondroudis, and C. R. Kagan, “Organic-inorganic electronics,” *IBM Journal of Research and Development*, vol. 45, no. 1. pp. 29–45, 2001.

[50] D. B. Mitzi, S. Wang, C. A. Feild, C. A. Chess, and A. M. Guloy, “Conducting Layered Organic-inorganic Halides Containing <110>-Oriented Perovskite

Sheets," *Science (80-.).*, vol. 267, no. 5203, pp. 1473–1476, Mar. 1995.

[51] A. Kojima, K. Teshima, Y. Shirai, and T. Miyasaka, "Novel Photoelectrochemical Cell with Mesoscopic Electrodes Sensitized by Lead-halide Compounds (5)," *Meet. Abstr.*, vol. MA2007-02, no. 8, pp. 352–352, 2007.

[52] S. Colella, E. Mosconi, P. Fedeli, A. Listorti, F. Gazza, F. Orlandi, P. Ferro, T. Besagni, A. Rizzo, G. Calestani, G. Gigli, F. De Angelis, and R. Mosca, "MAPbI $_{3-x}$ Cl $_{x}$ Mixed Halide Perovskite for Hybrid Solar Cells: The Role of Chloride as Dopant on the Transport and Structural Properties," *Chem. Mater.*, vol. 25, no. 22, pp. 4613–4618, Nov. 2013.

[53] H. Yu, F. Wang, F. Xie, W. Li, and J. Chen, "The Role of Chlorine in the Formation Process of 'CH3NH3PbI3-xClx' Perovskite," *Adv. Funct.*, 2014.

[54] S. Kulkarni, T. Baikie, P. Boix, and N. Yantara, "Band-gap tuning of lead halide perovskites using a sequential deposition process," *J. Mater.*, 2014.

[55] G. Eperon, S. Stranks, and C. Menelaou, "Formamidinium lead trihalide: a broadly tunable perovskite for efficient planar heterojunction solar cells," *Energy &*, 2014.

[56] S. Lv, S. Pang, Y. Zhou, N. Padture, and H. Hu, "One-step, solution-processed formamidinium lead trihalide (FAPbI (3− x) Cl x) for mesoscopic perovskite–polymer solar cells," *Phys. Chem.*, 2014.

[57] N. J. Jeon, J. H. Noh, W. S. Yang, Y. C. Kim, S. Ryu, J. Seo, and S. Il Seok, "Compositional engineering of perovskite materials for high-performance solar cells," *Nature*, vol. 517, no. 7535, pp. 476–480, Jan. 2015.

[58] S. D. Stranks, G. E. Eperon, G. Grancini, C. Menelaou, M. J. P. Alcocer, T. Leijtens, L. M. Herz, A. Petrozza, and H. J. Snaith, "Electron-Hole Diffusion Lengths Exceeding 1 Micrometer in an Organometal Trihalide Perovskite Absorber," *Science (80-.).*, vol. 342, pp. 341–344, 2013.

[59] Q. Dong, Y. Fang, Y. Shao, P. Mulligan, J. Qiu, L. Cao, and J. Huang, "Electron-hole diffusion lengths >175 μm in solution grown CH3NH3PbI3 single crystals," *Science (80-.).*, 2015.

[60] T. C. Sum and N. Mathews, "Advancements in perovskite solar cells: photophysics behind the photovoltaics," *Energy Environ. Sci.*, vol. 7, no. 8, pp. 2518–2534, May 2014.

[61] C. Li, X. Lu, W. Ding, L. Feng, Y. Gao, and Z. Guo, "Formability of ABX_3 (X = F, Cl, Br, I) halide perovskites," *Acta Crystallogr. Sect. B Struct. Sci.*, vol. 64, no. 6, pp. 702–707, Dec. 2008.

[62] W.-J. W. Yin, J.-H. J. Yang, J. Kang, Y. Yan, and S.-H. Wei, "Halide Perovskite Materials for Solar Cells: A Theoretical Review," *J. Mater. Chem. A*, vol. 3, no. 17, p. Advance, 2015.

[63] C. C. Stoumpos, C. D. Malliakas, and M. G. Kanatzidis, "Semiconducting Tin and Lead Iodide Perovskites with Organic Cations: Phase Transitions, High Mobilities, and Near-Infrared Photoluminescent Properties," *Inorg. Chem.*, vol. 52, no. 15, pp. 9019–9038, Aug. 2013.

[64] D. B. Mitzi, C. A. Feild, W. T. A. Harrison, and A. M. Guloy, "Conducting tin halides with a layered organic-based perovskite structure," *Nature*, vol. 369, no. 6480, pp. 467–469, Jun. 1994.

[65] T. Baikie, Y. Fang, J. M. Kadro, M. Schreyer, F. Wei, S. G. Mhaisalkar, M. Graetzel,

and T. J. White, “Synthesis and crystal chemistry of the hybrid perovskite (CH3NH3)PbI3 for solid-state sensitised solar cell applications,” *J. Mater. Chem. A*, vol. 1, no. 18, p. 5628, 2013.

[66] M. A. Green, A. Ho-Baillie, and H. J. Snaith, “The emergence of perovskite solar cells,” *Nat. Photonics*, vol. 8, no. 7, pp. 506–514, Jun. 2014.

[67] J. Yin, D. Cortecchia, A. Krishna, S. Chen, N. Mathews, A. C. Grimsdale, and C. Soci, “Interfacial charge transfer anisotropy in polycrystalline lead iodide perovskite films,” *J. Phys. Chem. Lett.*, vol. 6, no. 8, pp. 1396–1402, 2015.

[68] W.-J. Yin, T. Shi, and Y. Yan, “Unusual defect physics in CH3NH3PbI3 perovskite solar cell absorber,” *Appl. Phys. Lett.*, vol. 104, no. 106, pp. 81902–221104, 2014.

[69] W. Kong, Z. Ye, Z. Qi, B. Zhang, M. Wang, A. Rahimi-Iman, and H. Wu, “Characterization of an abnormal photoluminescence behavior upon crystal-phase transition of perovskite CH3NH3PbI3,” *Phys. Chem. Chem. Phys.*, vol. 17, no. 25, pp. 16405–16411, 2015.

[70] T. Oku, “Crystal Structures of CH3NH3PbI3 and Related Perovskite Compounds Used for Solar Cells,” in *Solar Cells - New Approaches and Reviews*, InTech, 2015.

[71] A. Poglitsch and D. Weber, “Dynamic disorder in methylammoniumtrihalogenoplumbates (II) observed by millimeter-wave spectroscopy,” *J. Chem. Phys.*, vol. 87, no. 11, p. 6373, 1987.

[72] N. Onoda-Yamamuro, T. Matsuo, and H. Suga, “Calorimetric and IR spectroscopic studies of phase transitions in methylammonium trihalogenoplumbates (II)†,” *J. Phys. Chem. Solids*, vol. 51, no. 12, pp. 1383–1395, 1990.

[73] Y. Kawamura, H. Mashiyama, and K. Hasebe, “Structural Study on Cubic–Tetragonal Transition of $CH_3NH_3PbI_3$,” *J. Phys. Soc. Japan*, vol. 71, no. 7, pp. 1694–1697, Jul. 2002.

[74] G. Rainò, G. Nedelcu, L. Protesescu, M. I. Bodnarchuk, M. V. Kovalenko, R. F. Mahrt, and T. Stöferle, “Single Cesium Lead Halide Perovskite Nanocrystals at Low Temperature: Fast Single-Photon Emission, Reduced Blinking, and Exciton Fine Structure,” *ACS Nano*, vol. 10, no. 2, pp. 2485–2490, Feb. 2016.

[75] K. Heidrich, H. Künzel, and J. Treusch, “Optical properties and electronic structure of CsPbCl3 and CsPbBr3,” *Solid State Commun.*, vol. 25, no. 11, pp. 887–889, Mar. 1978.

[76] R. J. Sutton, G. E. Eperon, L. Miranda, E. S. Parrott, B. A. Kamino, J. B. Patel, M. T. Hörantner, M. B. Johnston, A. A. Haghighirad, D. T. Moore, and H. J. Snaith, “Bandgap-Tunable Cesium Lead Halide Perovskites with High Thermal Stability for Efficient Solar Cells,” *Adv. Energy Mater.*, vol. 6, no. 8, 2016.

[77] Y. H. Chang and C. H. Park, “First-principles Study of the Structural and the Electronic Properties of the Lead-halide-based Inorganic-organic Perovskites (CH3NH3) PbX3 and CsPbX3(X=Cl, Br, I),” *J. Korean Phys. Soc.*, vol. 44, no. 4, pp. 889–893, 2004.

[78] C. C. Stoumpos, C. D. Malliakas, J. A. Peters, Z. Liu, M. Sebastian, J. Im, T. C. Chasapis, A. C. Wibowo, D. Y. Chung, A. J. Freeman, B. W. Wessels, and M. G. Kanatzidis, “Crystal Growth of the Perovskite Semiconductor CsPbBr3 : A New Material for High-Energy Radiation Detection,” *Cryst. Growth Des.*, vol. 13, no. 7, pp. 2722–2727, Jul. 2013.

[79] L. Na Quan, M. Yuan, R. Comin, O. Voznyy, E. M. Beauregard, S. Hoogland, A. Buin,

A. R. Kirmani, K. Zhao, A. Amassian, D. Ha Kim, and E. H. Sargent, “Ligand-Stabilized Reduced-Dimensionality Perovskites,” *J. Am. Chem. Soc.*, vol. 138, no. 8, pp. 2649–2655, 2016.

[80] M. Yuan, L. Na Quan, R. Comin, G. Walters, R. Sabatini, O. Voznyy, S. Hoogland, Y. Zhao, E. M. Beauregard, P. Kanjanaboos, Z. Lu, D. Ha Kim, and E. H. Sargent, “Perovskite energy funnels for efficient light-emitting diodes,” *Nat. Nanotechnol.*, vol. 11, no. 10, pp. 872–877, 2016.

[81] D. Zhang, S. W. Eaton, Y. Yu, L. Dou, and P. Yang, “Solution-Phase Synthesis of Cesium Lead Halide Perovskite Nanowires,” *J. Am. Chem. Soc.*, vol. 137, no. 29, pp. 9230–9233, Jul. 2015.

[82] L. Protesescu, S. Yakunin, M. I. Bodnarchuk, F. Krieg, R. Caputo, C. H. Hendon, R. X. Yang, A. Walsh, and M. V. Kovalenko, “Nanocrystals of Cesium Lead Halide Perovskites (CsPbX3 , X = Cl, Br, and I): Novel Optoelectronic Materials Showing Bright Emission with Wide Color Gamut,” *Nano Lett.*, vol. 15, no. 6, pp. 3692–3696, Jun. 2015.

[83] C. C. Stoumpos, D. H. Cao, D. J. Clark, J. Young, J. M. Rondinelli, J. I. Jang, J. T. Hupp, and M. G. Kanatzidis, “Ruddlesden–Popper Hybrid Lead Iodide Perovskite 2D Homologous Semiconductors,” *Chem. Mater.*, vol. 28, no. 8, pp. 2852–2867, Apr. 2016.

[84] Attolight, “Allalin 4027 Chronos User Guide,” 2016.

[85] S. Sonderegger, D. Gachet, and J. Berney, “High-Resolution Quantitative CL for Defect Metrology in Semiconductors,” 2016.

[86] GATAN, “High spatial resolution cathodoluminescence | Gatan, Inc.” [Online]. Available: http://www.gatan.com/high-spatial-resolution-cathodoluminescence. [Accessed: 24-Mar-2017].

[87] G. El-Hajje, C. Momblona, L. Gil-Escrig, J. Avila, T. Guillemot, J.-F. Guillemoles, M. Sessolo, H. J. Bolink, and L. Lombez, “Quantification of spatial inhomogeneity in perovskite solar cells by hyperspectral luminescence imaging,” *Energy Environ. Sci.*, vol. 9, no. 7, pp. 2286–2294, 2016.

[88] W. Peng, J. Yin, K.-T. Ho, O. Ouellette, M. De Bastiani, B. Murali, O. El Tall, C. Shen, X. Miao, J. Pan, E. Alarousu, J.-H. He, B. S. Ooi, O. F. Mohammed, E. Sargent, and O. M. Bakr, “Ultralow Self-Doping in Two-dimensional Hybrid Perovskite Single Crystals,” *Nano Lett.*, vol. 17, no. 8, pp. 4759–4767, Aug. 2017.

[89] Y. Zhang, Y. Liu, Z. Yang, and S. F. Liu, “High-quality perovskite MAPbI3 single crystals for broad-spectrum and rapid response integrate photodetector,” *J. Energy Chem.*, Nov. 2017.

[90] Antonie J.W.G. Visser and Olaf J. Rolinski, “BASIC PHOTOPHYSICS.” [Online]. Available: http://photobiology.info/Visser-Rolinski.html. [Accessed: 14-May-2017].

[91] S. C. Dixon, D. O. Scanlon, C. J. Carmalt, and I. P. Parkin, “n-Type doped transparent conducting binary oxides: an overview,” *J. Mater. Chem. C*, vol. 4, no. 29, pp. 6946–6961, 2016.

[92] D. W. deQuilettes, W. Zhang, V. M. Burlakov, D. J. Graham, T. Leijtens, A. Osherov, V. Bulović, H. J. Snaith, D. S. Ginger, and S. D. Stranks, “Photo-induced halide redistribution in organic–inorganic perovskite films,” *Nat. Commun.*, vol. 7, p. 11683, May 2016.

[93] S.-Y. Chiam, R. Singh, C. Rockstuhl, F. Lederer, W. Zhang, and A. A. Bettiol,

"Analogue of electromagnetically induced transparency in a terahertz metamaterial," *Phys. Rev. B*, vol. 80, no. 15, p. 153103, Oct. 2009.

[94] R. A. Shelby, D. R. Smith, and S. Schultz, "Experimental Verification of a Negative Index of Refraction," *Science (80-.).*, vol. 292, no. 5514, pp. 77–79, Apr. 2001.

[95] H.-T. Chen, W. J. Padilla, J. M. O. Zide, A. C. Gossard, A. J. Taylor, and R. D. Averitt, "Active terahertz metamaterial devices," *Nature*, vol. 444, no. 7119, pp. 597–600, Nov. 2006.

[96] B. Gholipour, G. Adamo, D. Cortecchia, H. N. S. Krishnamoorthy, M. D. Birowosuto, N. I. Zheludev, and C. Soci, "Organometallic Perovskite Metasurfaces," *Adv. Mater.*, vol. 29, no. 9, p. 1604268, Mar. 2017.

[97] S. M. Sze and K. K. Ng, *Physics of Semiconductor Devices*, 3rd ed. .

[98] E. Edri, S. Kirmayer, S. Mukhopadhyay, K. Gartsman, G. Hodes, and D. Cahen, "Elucidating the charge carrier separation and working mechanism of CH3NH3PbI3−xClx perovskite solar cells," *Nat. Commun.*, vol. 5, pp. 2920–2927, Mar. 2014.

[99] J. Berney, "The Attolight CL System," 2013.

[100] D. C. Harris, *Quantitative Chemical Analysis*, 7th editio. W. H. Freeman and Company, 2007.

[101] R. Fulton, "Instrumental Analysis: Spectrophotometric Methods."